The Astrophysical Journal, 965:165 (18pp), 2024 April 20 https://doi.org/10.3847/1538-4357/ad2857

The Initial Conditions of Clustered Core Collapse: Multiwavelength Analysis of Oph A SM1N and N6 at 100 au Resolution

Rachel K. Friesen[1], Tyler L. Bourke[2], Paola Caselli[3], James Di Francesco[4], Zhi-Yun Li[5], and Jaime E. Pineda[3]
[1] Department of Astronomy & Astrophysics, University of Toronto, 50 St. George Street, Toronto, ON M5S 3H4, Canada; rachel.friesen@utoronto.ca
[2] SKA Observatory, Jodrell Bank, Lower Withington, Macclesfield, Cheshire, SK11 9FT, UK
[3] Centre for Astrochemical Studies, Max-Planck-Institut für extraterrestrische Physik, Gießenbachstraße 1, 85749 Garching bei München, Germany
[4] NRC Herzberg Astronomy and Astrophysics, 5071 West Saanich Road, Victoria, BC V9E 2E7, Canada
[5] Department of Astronomy, University of Virginia, Charlottesville, VA 22904, USA
Received 2023 July 28; revised 2024 January 30; accepted 2024 February 10; published 2024 April 17

Abstract

We present new Atacama Large Millimeter/submillimeter Array (ALMA) continuum and NH_2D, N_2D^+, and H_2D^+ line emission at matched, ∼100 au resolution toward the dense star-forming cores SM1N and N6 within the Ophiuchus molecular cloud. We determine the density and temperature structure of SM1N based on radiative transfer modeling and simulated observations of the multiwavelength continuum emission at 0.8, 2, and 3 mm. We show that SM1N is best fit by either a broken power-law or Plummer-like density profile with high central densities ($n \sim 10^8$ cm^{-3}), and an inner transition radius of only ∼80–300 au. The free-fall time of the inner region is only a few $\times 10^3$ yr. The continuum modeling rules out the presence of an embedded first hydrostatic core (FHSC) or protostar. SM1N is therefore a dynamically unstable but still starless core. We find that NH_2D is likely depleted at high densities within SM1N. The nonthermal velocity dispersions increase from NH_2D to N_2H^+ and H_2D^+, possibly tracing increasing (but still subsonic) infall speeds at higher densities as predicted by some models of starless core contraction. Toward N6, we confirm the previous ALMA detection of a faint, embedded point source (N6-mm) in 0.8 mm continuum emission. NH_2D and N_2D^+ avoid N6-mm within ∼100 au, while H_2D^+ is not strongly detected toward N6. The distribution of these tracers is consistent with heating by a young, warm object. N6-mm thus remains one of the best candidate FHSCs detected so far, although its observed (sub)millimeter luminosity remains below predictions for FHSCs.

Unified Astronomy Thesaurus concepts: Star formation (1569); Astrochemistry (75); Chemical abundances (224); Protostars (1302); Young stellar objects (1834)

1. Introduction

Low-mass stars form from the collapse of cold, dense molecular cores in star-forming clouds (for a review, see Pineda et al. 2023). While starless, the radial density profile determined observationally for gravitationally or pressure-bound dense cores is often flat at radii less than some value, and then decreases proportional to r^{-2} at larger radii (e.g., Ward-Thompson et al. 1999; Bacmann et al. 2000; Alves et al. 2001). Cores apparently in equilibrium have been well described as Bonnor–Ebert spheres (BES), with the density structure constrained by the balance between thermal pressure and self-gravity and external pressure, resulting in this radial density form.

As an unstable core contracts, the density profile remains similar in shape, where the central density increases while the transition radius decreases (Larson 1969; Foster & Chevalier 1993), thus approaching the $\rho \propto r^{-2}$ density profile of a singular isothermal sphere (SIS; Keto & Caselli 2010). This progression remains true in global-gravitational-collapse models, where core-density profiles evolve toward the SIS solution (Gómez et al. 2021). Post-formation of an accreting object, the SIS model predicts a transition radius that moves outward with time, shifting back to a more shallow, $\rho \propto r^{-3/2}$ density profile at small r as collapse proceeds from the inside-out (Shu 1977). The protostellar source MMS-1 in L1521F shows such a transition (Tokuda et al. 2016). Cores with density profiles that show transitions at small radii are thus highly evolved, either pre- or just post-formation of an accreting object at their center. One such starless object is the isolated core L1544, with a central density $n \gtrsim 10^6$ cm^{-3} within a transition radius of only $r \sim 1400$ au (Caselli et al. 2019). Determining accurately the density profiles of such objects are thus the first steps to examining the earliest stages of protostellar formation.

Another such highly evolved object is the dense core SM1N within the Ophiuchus molecular cloud. The L1688 region in the Ophiuchus molecular cloud is one of the nearest young stellar-cluster-forming environments ($d = 137$ pc; Ortiz-León et al. 2017). Within L1688, the Oph A clump is a ridge-like feature that contains $\sim 23\,M_\odot$ of dust and gas, multiple compact and dense cores (Motte et al. 1998), and at least six protostars (Friesen et al. 2018), including the prototypical Class 0 protostar VLA 1623 (André et al. 1990). Oph A itself is thus forming a small group or cluster of protostars, within the general L1688 cluster. Friesen et al. (2018) proposed that the radial density profile of the SM1N core in the Ophiuchus A star-forming filament was proportional to $r^{-1.3}$ at radii $r \lesssim 200$ au. Determined via Atacama Large Millimeter/submillimeter Array (ALMA) continuum observations at ∼80 au (0.″6) resolution, this suggests that the apparently starless core is nevertheless gravitationally unstable and likely undergoing collapse. An additional evolved core in Oph A, N6, was previously thought to be starless (Di Francesco et al. 2004; Bourke et al. 2012), but was shown by Friesen et al. (2018) to contain a faint point source in ∼1 mm continuum emission. Neither source showed

evidence for the bipolar outflows that would be expected from a protostellar object, although outflow identification is complicated toward N6 due to its proximity to the substantial, narrow outflow originating from VLA 1623. Given their observed structure, lack of strong detections at short wavelengths, and lack of clear bipolar outflows with velocities greater than a few kilometers per second, SM1N and N6 were identified as the best candidates of first hydrostatic cores (FHSCs) of the handful of proposed sources yet detected (Young et al. 2019), along with several more recent candidates (Fujishiro et al. 2020; Maureira et al. 2020).

At high densities ($n \gtrsim 10^6$ cm^{-3}) and low temperatures ($T \lesssim 20$ K), molecular species such as CO are depleted from the gas phase due to freezing out onto dust grains, forming icy mantles (e.g., Bergin & Tafalla 2007). Concurrently, the abundance of H_2D^+ is increased via reactions between H_3^+ and HD, which occur preferentially in the forward direction at these temperatures (Roberts & Millar 2000). Enhanced abundances of deuterated forms of typical dense-gas-tracing molecules like NH_3 and N_2H^+ follow via reactions with H_2D^+. At very high densities, H_2D^+ and its multiply deuterated isotopologues may be the most abundant species remaining in the gas phase, as molecules containing heavier elements deplete onto dust grains (Walmsleyet al. 2004), including NH_3 and NH_2D (Pineda et al. 2022; Caselli et al. 2022). Once a protostar forms and warms its surroundings above $T \sim 20$ K, however, the abundances of H_2D^+ and other deuterated species decrease as increased temperatures allow the desorption of CO from dust grains. Deuterated species, particularly H_2D^+, are therefore key tracers of the physical conditions of dense cores on the cusp of gravitational collapse.

Here, we present ALMA observations toward SM1N and N6 of emission from the dust continuum emission at 3, 2, and 0.8 mm, as well as from dense-gas-tracing molecular lines, including the deuterated species NH_2D, N_2D^+, and H_2D^+ at matched, $\sim 0\farcs85 \times 0\farcs65$ ($\sim$100 au) resolution. Critical densities for the lines chosen range from 6.5×10^4 cm^{-3} (NH_2D; Daniel et al. 2014) through $\sim 10^5$ cm^{-3} (H_2D^+; Hugo et al. 2009) to 8.7×10^5 cm^{-3} (N_2D^+; Redaelli et al. 2019). We thus use the line-emission distribution and spectral-fitting results to constrain the density, temperature, and kinematics of the cores at high densities and small radii. Based on the ALMA-detected continuum emission from $\sim$3 to $\sim$850 μm wavelengths, we model the radial volume density and temperature structure of SM1N using the 3D Monte Carlo radiative transfer code RADMC-3D (Dullemond et al. 2012) to determine the radial density profile, and assess whether internal heating (i.e., protostellar) sources are needed to explain the observed emission.

In Section 2, we discuss the ALMA observations and imaging of the continuum and line data. We present the resulting continuum images and initial discussion in Section 3. We fit the observed line data in Section 4, using hyperfine modeling for the NH_2D and N_2D^+ lines. We perform radiative transfer modeling of the continuum in Section 5, where we use a grid of density profiles and a range of central densities to determine the predicted temperature profiles. We then simulate ALMA observations of the results, using the telescope configuration and *uv* coverage of our actual observations presented here. In Section 6, we analyze jointly the continuum and line results. We show that SM1N is a starless core undergoing dynamic, gravitational collapse, while N6 contains a compact source that remains one of the best FHSC candidates thus discovered. We summarize our findings in Section 7.

2. Observations

The ALMA data newly presented here were obtained as part of the Cycle 6 project 2018.1.00935.S and Cycle 5 project 2017.1.01006.S (PI: R. Friesen). Observations were performed over a range of dates between 2018 January and 2019 April. We also make use of observations toward the same sources from the Cycle 2 project 2013.1.00937.S (PI: R. Friesen), published in Friesen et al. (2018).

Each source was observed with a single pointing in continuum and line emission at ALMA Bands 3, 4, and 7. The central frequency, spectral resolution, and dense-gas-tracing lines targeted are listed in Tables 1 and 2. Observations were performed over a range of ALMA configurations to provide matched angular resolution and matched sensitivity to larger angular scales. Additional carbon-bearing species were also observed simultaneously; these will be presented and discussed in a later paper.

At Bands 3 and 4, two 12 m configurations were used. To achieve the same sensitivity to extended structure at Band 7 as at Bands 3 and 4, observations were performed with one 12 m configuration and separately with the 7 m ALMA Compact Array. We list in Table 1 the final synthesized beam and maximum recoverable scale ($\theta_{\rm MRS}$) at each band. The synthesized beam size depends on choices made in the deconvolution and imaging process, described further below, while $\theta_{\rm MRS}$ is calculated from the minimum baselines in final measurement sets.

2.1. Continuum Emission

Calibration and imaging were done using the Common Astronomy Software Applications (CASA) package (CASA Team et al. 2022). All data were pipeline reduced in CASA v5.4.

Continuum images for each target were made with the `tclean` task in CASA v5.4, using multifrequency synthesis to combine data from both 12 m configurations (or in the case of Band 7, the 12 and 7 m arrays), and all 1.875 GHz wide continuum spectral windows (two windows each at Bands 3 and 4, and three windows at Band 7). For all data sets, a Briggs weighting with a robustness parameter of 0.5 was used. We additionally performed multiscale cleaning on the SM1N data with scale sizes of 0, 1, and 3 times the synthesized beam size to better recover extended emission. The resulting synthesized beams are roughly $0\farcs85 \times 0\farcs65$ across all bands ($\sim 115 \times 90$ au at the distance to L1688). Details of the noise level achieved and the beam parameters for each source as a function of band are provided in Table 1. The resulting continuum images are shown in Figure 1. The figure also includes the ALMA Band 6 continuum images from Friesen et al. (2018) toward SM1N and N6, which have similar resolution ($\sim 0\farcs6$) but more limited sensitivity to larger-scale structures.

Hereafter, we will use the approximate wavelength of the continuum setup to describe the observations and analysis of the continuum emission at the different bands: 3 mm (Band 3), 2 mm (Band 4), and 0.8 mm (Band 7).

2.2. Line Emission

Details of the lines targeted in the ALMA observations are given in Table 2. To image both sources in all lines, the

Table 1
Details of Combined Continuum Observations

Source	ALMA Band	Freq. (GHz)	λ (mm)	rms (μJy bm^{-1})	θ_{maj} (arcsec)	θ_{min} (arcsec)	PA (deg)	θ_{MRS} (arcsec)
SM1N	3	98.944	3	37	0.87	0.67	−89.9	23.2
	4	149.804	2	85	0.84	0.59	−80.6	17.0
	7	364.883	0.8	333	0.84	0.58	88.2	17.5
N6	3	98.944	3	18	0.86	0.67	89.7	23.2
	4	149.804	2	40	0.87	0.64	−80.2	17.0
	7	364.883	0.8	140	0.84	0.58	88.0	17.5

Table 2
Details of Spectral-line Observations

Species	Transition	Rest freq. (GHz)	Δv (km s^{-1})	rms (mJy bm^{-1})	rms (K)
oNH_2D	1_{11}–1_{01}	85.92626	0.12	3	0.61
N_2D^+	2–1	154.21701	0.08	2.5	0.39
H_2D^+	$1_{(10)}$–$1_{(11)}$	372.42139	0.11	10	0.18
N_2H^+	4–3	372.67249	0.11	10	0.18

continuum emission was identified in line-free spectral channels and subtracted from the spectral windows in the *uv* plane. The continuum-subtracted visibilities were then imaged over the spectral range of interest with the same robustness parameter used for the continuum images. We used multiscale cleaning for both sources and all lines to recover better the extended emission. We additionally applied CASA's automated masking algorithm to identify more robustly the regions containing line emission in each spectral channel (Kepley et al. 2020). We found that the automated masking algorithm correctly identified regions with emission in each frequency channel with some adjustment of the default algorithm parameters for different lines and sources. Final velocity resolutions varied by line and are listed in Table 2, but are generally $\sim$0.1 km s^{-1}, and the emission lines toward both sources are spectrally resolved. The final synthesized beams match closely those for the continuum maps at similar frequencies.

The resulting cubes were corrected for the primary beam, and the amplitudes converted to brightness temperature. We show in Figure 2 the emission from the dense-gas tracers listed above, integrated over the extent of the emission in velocity (including hyperfine components, where present; we discuss this further in Section 4). We additionally overlay contours showing the 0.8 mm continuum, noting that the primary beam at this wavelength covers only the central component in some of the line maps. Toward N6, we furthermore tapered the H_2D^+ data to a final angular resolution of 1.″5 to improve sensitivity, as the H_2D^+ emission was undetected toward this source at the original resolution.

3. Continuum Results

Here, we discuss the continuum emission of both compact and extended sources detected at the observed wavelengths. More detailed radiative transfer analysis of the extended emission toward SM1N is described in Section 5.

3.1. (Sub)millimeter Continuum Detections

Figure 1 shows the continuum emission across all observed ALMA wavelengths toward SM1N and N6. We include the observations at 3, 2, and 0.8 mm newly described here, as well as continuum data at Band 6 (hereafter 1 mm) from Friesen et al. (2018). Both compact and extended continuum emission is detected within the primary beam toward both sources and across all frequencies observed with ALMA.

The main continuum feature toward SM1N, seen at all wavelengths, is an elongated structure with a compact, but not point-like, emission peak near the northwestern end. In the larger fields of view, fainter, extended emission follows the line of the Oph A ridge to the northwest and southeast. The contrast between the emission peak and extended emission increases with decreasing wavelength. In the 3 mm observations, the wider field of view contains two bright compact sources: SM1 to the south, and GY30 to the northwest (labeled in Figure 1). Previous ALMA observations of SM1 suggest the continuum emission reveals a compact disk around a young protostar (Friesen et al. 2014, 2018; Kawabe et al. 2018). GY30 (also Oph-emb9) has been identified as a Class I object (Greene & Young 1992; Enoch et al. 2009). SM1 and GY30 are outside of the field of view at the other observed wavelengths.

Toward N6, continuum emission is detected near the pointing center at 2, 1, and 0.8 mm. At 2 and 0.8 mm, faint extended emission surrounds a point-like source, N6-mm, first detected at 1 mm in Friesen et al. (2018). Extended 1 mm emission of $\sim$3000 × 1400 au extent was previously detected at $\lesssim$300 au resolution (Bourke et al. 2012). This is more extended than in our data, but in good location agreement. The extended emission was also previously detected at 1 mm when the data were tapered to a slightly larger beam (Friesen et al. 2018, not shown here). At 3 mm, extended continuum is seen to the northwest, and coincides with the larger continuum ridge structure of Ophiuchus A. In addition, a compact continuum source is detected at 3 and 2 mm, also to the northwest but offset from the extended emission. This compact source, which we label N6-w in Figure 1, has not been identified in previous observations of N6 or Oph A, and is outside of the field of view at 1 and 0.8 mm. N6-w lies within the Oph A ridge as traced by single-dish continuum emission, but is offset from the dense gas as traced by, for example, N_2H^+ (Di Francesco et al. 2004).

3.2. Gaussian Fitting of N6-mm and Other Compact Continuum Sources

For the compact continuum emission sources, including N6-mm, we fit the emission peaks in the images with 2D Gaussians using the CASA task `imfit`, and determine the total flux in an elliptical aperture around each source matching the Gaussian fit parameters here and in previous papers. For N6-mm, we first remove the extended background emission by subtracting a median flux value in an elliptical annulus with inner and outer limits of 3 and 5 times the aperture axes, oriented with the position angle of the Gaussian fit. We list in Table 3 the fit results at each wavelength, including the location in R.A. and

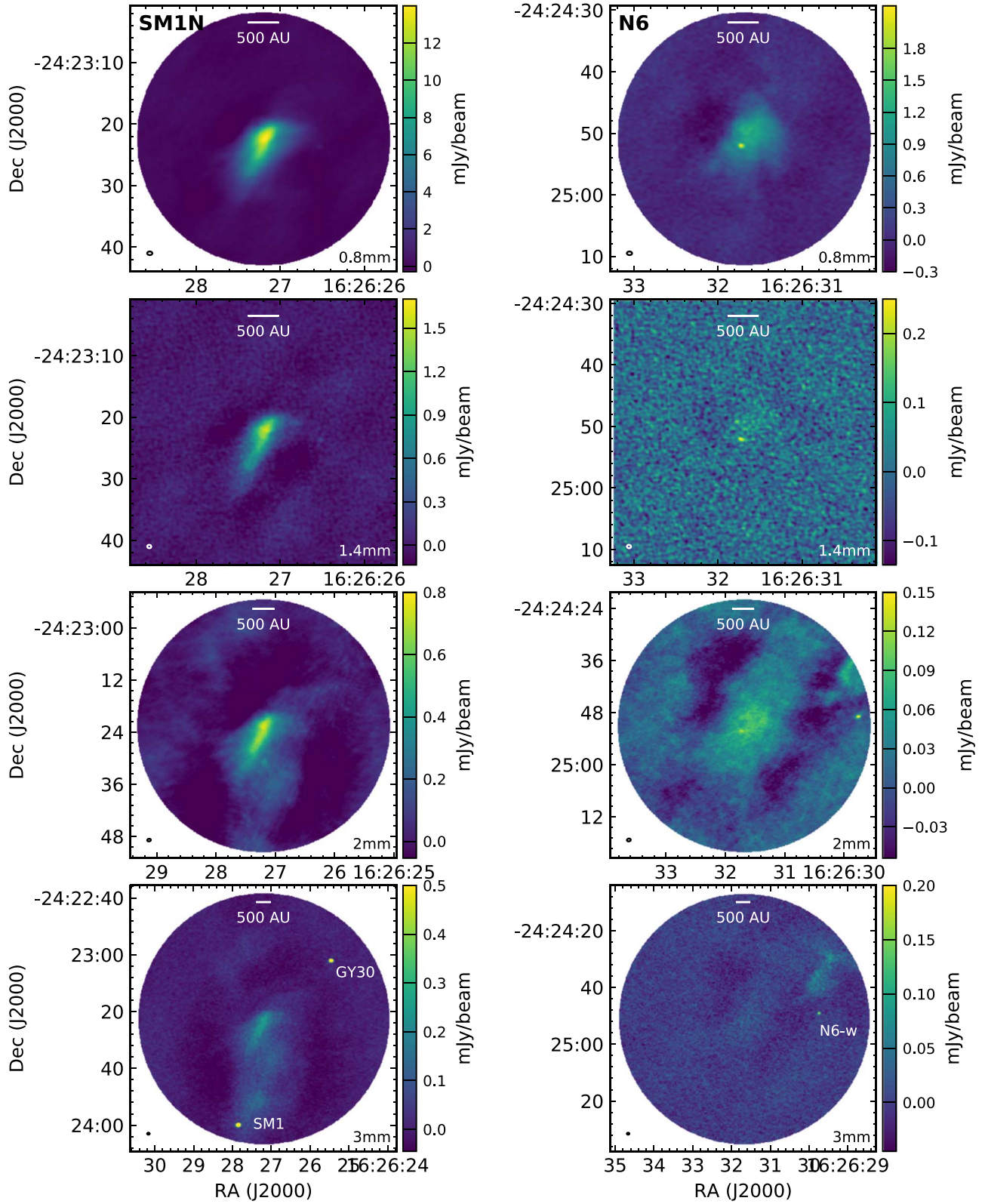

Figure 1. Continuum emission toward Oph A SM1N (left) and N6 (right) at 0.8, 1, 2, and 3 mm (top to bottom; ALMA). In each panel, the area imaged is limited to where the primary-beam gain is greater than 0.2. The resulting scale of each panel is shown by the scale bar. SM1N and N6 are centered in each panel. Additional continuum point sources are seen in the 3 mm images toward both sources, and additionally in the 2 mm image toward N6; at other wavelengths they are outside of the imaged area.

decl., the total flux S_ν and peak flux density I_ν, and the major and minor axes and position angle of the best-fit Gaussian model. For SM1 and N6-mm, the source locations agree with those found in Friesen et al. (2018).

For the compact sources detected at at least two wavelengths, we show in Figure 3 the resulting fluxes as a function of wavelength. The source fluxes span 2 orders of magnitude across the observed wavelengths. We include compact sources

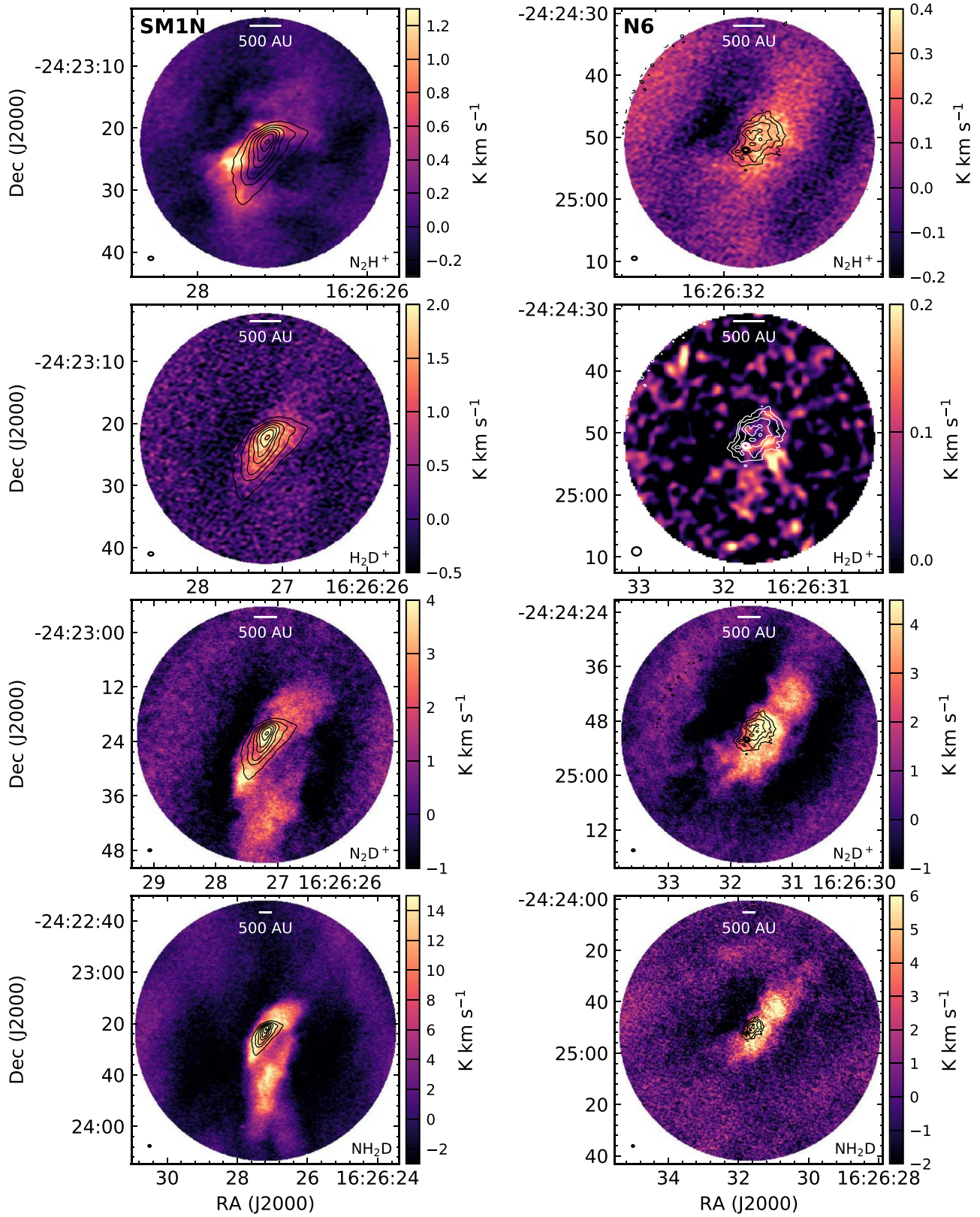

Figure 2. Integrated line intensity for the four molecular transitions discussed here toward SM1N (left) and N6 (right). In each panel, the area imaged is limited to where the primary-beam gain is greater than 0.2. The resulting scale of each panel is shown by the scale bar. SM1N and N6 are centered in each panel. The synthesized beam is shown in the lower left of each panel. Black contours show the ALMA 0.8 mm continuum toward each source. Toward SM1N, only N_2H^+ and H_2D^+ show integrated intensity peaks at the continuum peak, whereas both NH_2D and N_2H^+ appear optically thick at this location. Toward N6, the integrated intensity peaks for all lines are offset from the continuum point source, but are colocated with the extended continuum emission. H_2D^+ is only marginally detected toward N6 in a tapered beam.

Table 3
Compact-source Characteristics

Source	R.A. (J2000)	Decl. (J2000)	S_{B3} (mJy)	I_{B3} (mJy beam^{-1})	S_{B4} (mJy)	I_{B4} (mJy beam^{-1})	S_{B7} (mJy)	I_{B7} (mJy beam^{-1})	σ_{maj} (arcsec)	σ_{min} (arcsec)	PA (deg)	M ($M_\odot$)
GY30	16:26:25.47	−24:23:01.90	7.20(1)	6.61(3)	⋯	⋯	⋯	⋯	0.899(6)	0.707(4)	93.7(8)	0.086
SM1	16:26:27.86	−24:23:59.64	18.66(1)	16.17(4)	⋯	⋯	320(2)[a]	215(2)[a]	0.938(2)	0.748(2)	91.2(4)	0.233
N6-w	16:26:29.78	−24:24:48.76	0.40(1)	0.33(6)	1.00(3)	0.58(5)	⋯	⋯	0.9(5)	0.7(4)	101(119)	0.0043
N6-mm	16:26:31.73	−24:24:52.01	⋯	⋯	⋯	⋯	9.9(1)	1.8(1)	1.9(1)	1.4(1)	130(8)	0.0015

Notes. Angular sizes have not been deconvolved by the beam. All angular size measurements and mass estimates are calculated from 2D Gaussian fits to Band 3 (3 mm) images, apart from N6-mm, where the Band 7 (0.8 mm) images were used.
[a] Total flux and peak flux density from Friesen et al. (2014).

from Friesen et al. (2018) for reference. With the exception of N6-mm, the spectral energy distributions (SEDs) for the compact sources are more shallow than expected for typical interstellar medium (ISM) dust, with low values of the dust spectral index β that are likely the result of either grain growth or high-optical-depth effects. This includes the new source N6-w. Given the data in-hand, we cannot make a strong claim as to the nature of N6-w but note that it has similar size and emissivity spectral index as the known protostellar sources in the region, and is brighter than N6-mm by at least a factor of a few.

The dust spectral index toward N6-mm appears steeper and more consistent with ISM values, but we caution that the extended emission is much more prominent at shorter wavelengths and may not be removed perfectly by the annulus method used here, potentially resulting in a steeper spectral index.

If we assume the dust emission is optically thin, we can estimate the mass M for both the compact and extended continuum emission following

$$M = \frac{d^2\, S_\nu}{\kappa_\nu B_\nu(T_d)}, \quad (1)$$

where $d = 137.3$ pc is the source distance, κ_ν is the dust opacity at the frequency ν of the observations, and $B_\nu(T_d)$ is the Planck function at frequency ν and dust temperature T_d. The dust opacity $\kappa_\nu = \kappa_0(\nu/\nu_0)^\beta$. We assume the dust is characterized by a spectral index $\beta = 1.7$, and a gas-to-dust mass ratio of 100, with $\kappa_0 = 0.1$ cm^2 g^{-1} at a frequency $\nu_0 = 1000$ GHz.

For the compact sources, we assume dust temperatures $T_d = 15$ K. We calculate masses based on the 3 mm flux, which is least likely to be optically thick, apart from N6-mm, where we use the 0.8 mm flux since we do not detect the source at 3 mm. The compact-source masses are given in Table 3. For SM1, the resulting estimated mass is in agreement with Kirk et al. (2017), but is greater than in Friesen et al. (2018) by a factor of 2 (accounting for the different $T_d \sim 30$ K used), likely due to the uncertainties in β and the dust opacity at shorter wavelengths. The compact-source masses are generally consistent with disk masses in Class 0/I objects (Jørgensen et al. 2009; Enoch et al. 2011), with known protostellar sources GY30 and SM1 at the high end of typical mass range, and sources N6-mm and N6-w at the low end (Andersen et al. 2019).

Toward N6, we also estimate the mass in the more extended emission. We do not have direct measurements of the dust temperature at ∼100 au resolution, but at 15″–30″ (2000–4000 au) scales, Pon et al. (2009) showed that the dust and gas temperatures are $\sim 15-20$ K, potentially increasing toward the continuum peak. Allowing for T_d to vary between 30 and 15 K, we find the total mass of the extended 0.8 mm emission toward N6 is only $M \sim 0.01$–$0.02\ M_\odot$.

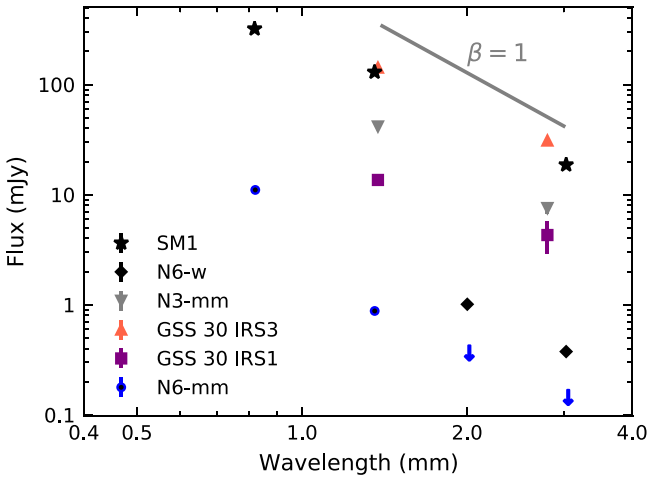

Figure 3. Total flux as a function of wavelength for all compact sources identified at at least two wavelengths in ALMA observations toward Oph A (this paper; Friesen et al. 2014, 2018). The gray line shows the expected slope for $\beta = 1$.

We give a more detailed analysis of the density and temperature profile of the extended SM1N emission in Section 5, but a similar calculation for SM1N gives a total mass $M \sim 0.16$ $M_\odot$, given the emission at 0.8 mm and a dust temperature of 15 K, matching previous mass measurements (Friesen et al. 2014).

4. Spectral-line Fitting and Analysis

4.1. Integrated Intensity Maps

We show in Figure 2 the integrated intensity of NH_2D, N_2D^+, H_2D^+, and N_2H^+ emission toward SM1N and N6. We detect all emission lines toward both sources; for N6, we detect the H_2D^+ emission in the tapered map only. The observed transitions of NH_2D, N_2H^+, and N_2D^+ contain hyperfine structure (hfs), and for these species we calculate the integrated intensity over all line components.

While all the above species are typically considered good tracers of cold, dense gas, we find a clear progression in how well the emission matches the continuum data in the integrated intensity maps. Toward SM1N, H_2D^+ and N_2D^+ show integrated intensity peaks at the continuum peak location, although N_2D^+ shows an additional peak to the southeast, and more extended emission than H_2D^+. Overall the integrated H_2D^+ emission matches exceptionally well the 0.8 mm

continuum, and we see no evidence of the H_2D^+ offset reported in Cycle 0 ALMA observations (Friesen et al. 2014). This may be due to the improvement in *uv* coverage and sensitivity in the newer data. The southeast N_2D^+ peak overlaps an extension from the peak of the SM1N core in the 2 mm continuum. While the continuum extends to this point, no additional continuum emission peak is seen, suggesting this is a region of enhanced N_2D^+ abundance. Further south of the SM1N emission peak, additional N_2D^+ emission overlaps with faint extended continuum emission visible at 3 and 2 mm. Two peaks are also seen in the NH_2D integrated intensity around the SM1N continuum, but the northwest NH_2D maximum is offset from the continuum peak, in contrast to N_2D^+. Further emission extends to the south of the continuum peak, overlapping and extending that seen in N_2D^+. In both the lines and the continuum, there is a narrow region of fainter emission between the more compact emission associated with SM1N and the extended emission that continues to the south and follows the extension of the Oph A ridge.

N_2H^+ 4–3 emission is a clear outlier, where the emission appears to line the northeast side of the core. The N_2H^+ line emission is significantly optically thick, affecting the spatial appearance in the integrated intensity map. The N_2H^+ emission extends toward the southern tip of the continuum source, although does not show an additional peak matching that detected in the N_2D^+ and NH_2D maps.

Toward N6, the integrated intensity of NH_2D, N_2D^+, and N_2H^+ appear to correlate well, but the integrated intensity peaks in all cases are offset from the compact continuum peak (N6-mm), and extend along the direction of the lower-level continuum emission. Similar offsets between the continuum and N_2D^+ 3–2 emission were identified at 15″ resolution (Pon et al. 2009). Two peaks are seen in the N_2D^+ and NH_2D integrated intensity maps, although the second peak is fainter in N_2D^+. The same two peaks were seen in N_2D^+ 3–2 at $\lesssim$300 au resolution (Bourke et al. 2012). A tentative detection of H_2D^+ offset from the southwest edge of the continuum may be real, but we note again that this data has been tapered to a larger beam to improve the signal. The N_2H^+ 4–3 line appears optically thick toward N6 (as is the N_2H^+ 3–2 line; Bourke et al. 2012), similar to SM1N, but the integrated intensity is in better agreement with the extended continuum and other molecular lines than in SM1N. The dense structures traced by N_2D^+ and NH_2D toward N6 are much more evident than in the continuum emission, where the extended emission near N6-mm is only barely detected at 2 mm and not at all at 3 mm.

4.2. Line Fitting

We show in Figure 4 the observed spectra for each line toward the continuum emission peaks of SM1N and N6, and their best-fit spectra as described below.

For H_2D^+, we fit a single Gaussian to the spectrum at each pixel across the map, and from this determine the line amplitude, the local standard of rest line-of-sight velocity, $v_{\rm LSR}$, and the velocity dispersion, σ_v, at each pixel where H_2D^+ is detected.

For NH_2D and N_2D^+, we fit the line emission, including the line hfs, using the `pyspeckit` package (Ginsburg & Mirocha 2011; Ginsburg et al. 2022). With `pyspeckit`, synthetic spectra are modeled assuming a constant excitation temperature $T_{\rm ex}$ for all hyperfine line components, and that the components are additionally characterized with a single $v_{\rm LSR}$ and velocity dispersion σ_v. The difference between the model and observed spectrum is minimized, and we obtain maps of the resulting $T_{\rm ex}$, line opacity τ summed over all hyperfine components, $v_{\rm LSR}$, and σ_v. For NH_2D, the line fitting takes into account the hyperfine splitting caused by the deuterium nucleus

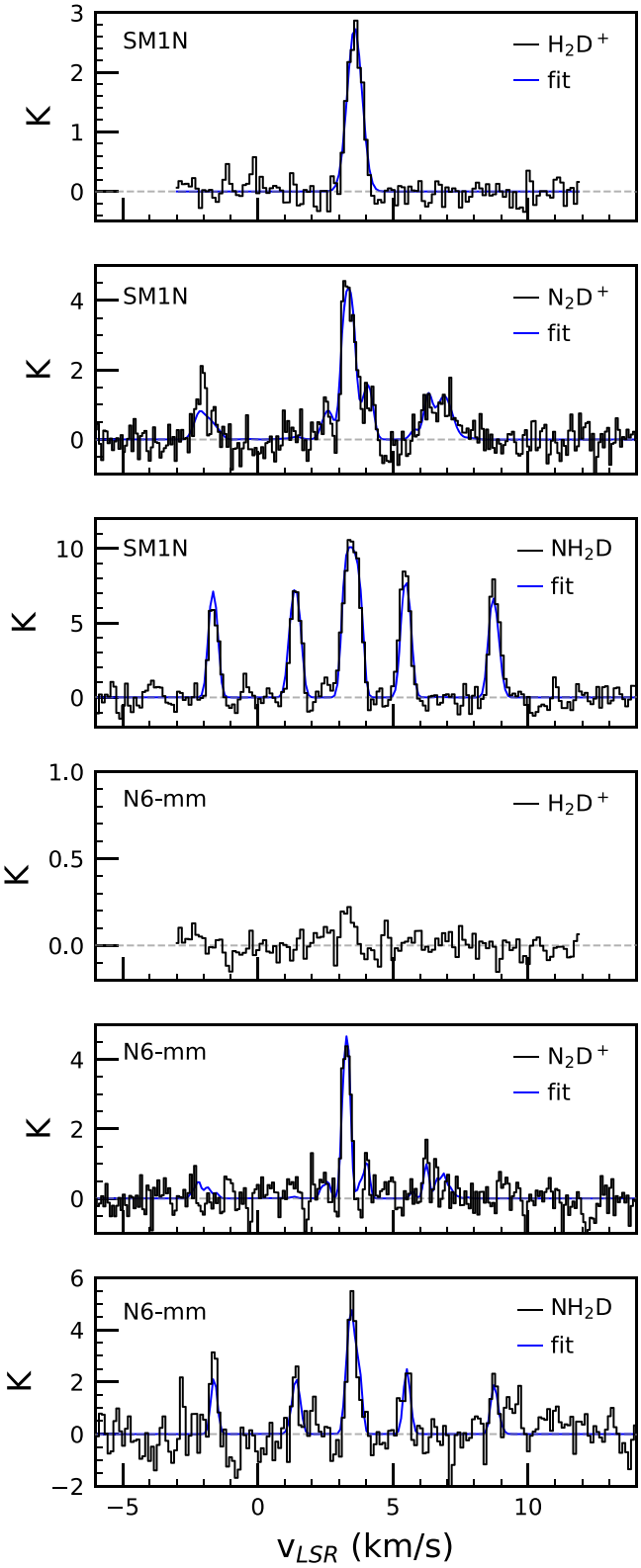

Figure 4. Examples of H_2D^+, N_2D^+, and NH_2D spectra toward the continuum emission peak of SM1N (top three panels) and N6 (bottom three panels). Best single Gaussian (H_2D^+) and hfs fits (N_2D^+, NH_2D) are overlaid in blue. Note that for N6, the line-emission peaks are offset from the continuum.

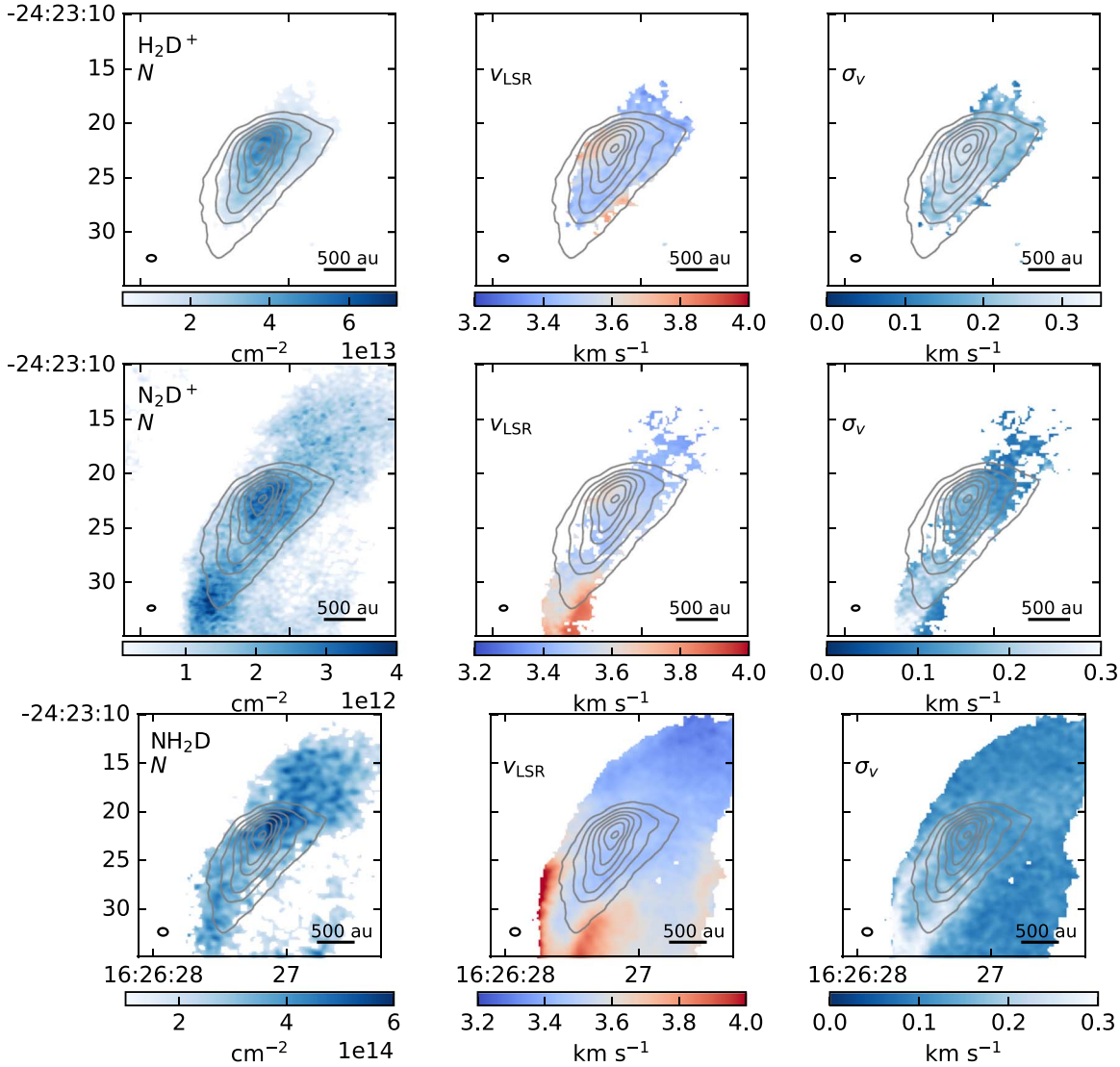

Figure 5. Total column density N (left), v_{LSR} (middle), and σ_v (right) as fit to H_2D^+ (top), N_2D^+ (middle), and NH_2D (bottom) toward SM1N, described in Section 4.2. Gray contours show continuum emission at 0.8 mm.

as calculated by Daniel et al. (2016). Line fits for all species were assessed and masked based on the uncertainties returned for each parameter.

We show the resulting v_{LSR} and σ_v distributions for H_2D^+, N_2D^+, and NH_2D toward SM1N and N6 in Figures 5 and 6, respectively. We also list in Table 4 the mean and standard deviation of all fit parameters within contours defined by the 0.8 mm continuum toward each source.

Toward both sources, the velocity patterns are very similar across all detected dense-gas-tracing species. Toward SM1N, the H_2D^+ and N_2D^+ in particular show the same v_{LSR} pattern: roughly constant velocity along the long axis of the continuum structure, with an apparent velocity gradient perpendicular to the long axis of the core, across the continuum peak. Additional changes in the v_{LSR} seen at the south and southwestern edges of the core in H_2D^+ and N_2D^+ are revealed to be part of larger-scale velocity gradients detected more broadly in NH_2D. Similar agreement is seen in N_2D^+ and NH_2D kinematics toward N6. In addition, both N_2D^+ and NH_2D show an apparent periodic variation of order $\sim$0.1 km s^{-1} in v_{LSR} in narrow stripes across N6. The shift in v_{LSR} values appears correlated with edges in the N_2D^+ integrated intensity (and similarly variations in $N(N_2D^+)$, derived below), where higher v_{LSR} is associated with lower integrated intensity values. This pattern is not seen at lower resolution (Bourke et al. 2012). The range of v_{LSR} is greater by a factor of 2 in SM1N compared with N6.

The observed velocity dispersions are also similar across all three species toward both sources, and are consistently narrow, with N6 showing more narrow line widths on average than SM1N ($\sigma_v \sim 0.1$ km s^{-1} and $\sigma_v \sim 0.15$ km s^{-1}, respectively, for N_2D^+ and NH_2D). This is consistent with single-dish observations, which identified N6 as a site of extremely narrow line widths within Oph A (Di Francesco et al. 2004), and is in agreement with previous high-resolution observations (Bourke et al. 2012). Intriguingly, although the integrated intensity maps show both N_2D^+ and NH_2D avoid the compact continuum peak N6-mm, there is no clear increase in σ_v seen in either line in the vicinity.

Toward SM1N, we found an offset between the NH_2D moment map peak and the continuum peak. We find that the NH_2D emission is optically thick toward the continuum peak and in the emission to the northwest. Total NH_2D line opacities

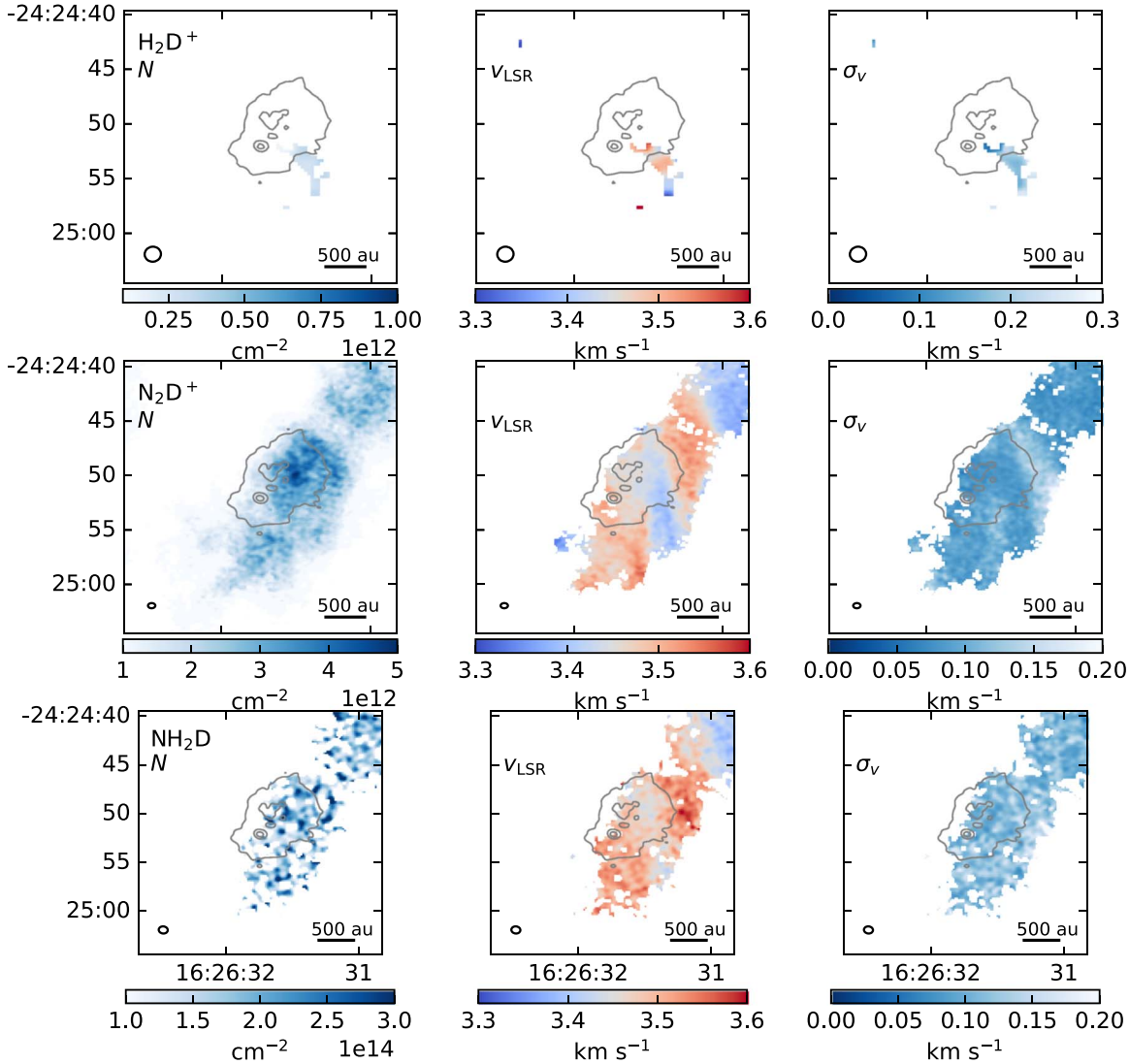

Figure 6. Total column density N (left), $v_{\rm LSR}$ (middle), and σ_v (right) as fit to H_2D^+ (top), N_2D^+ (middle), and NH_2D (bottom) toward N6, described in Section 4.2. Gray contours show continuum emission at 0.8 mm.

(summed over the hyperfine components) are ∼15 at the continuum peak, and excitation temperatures $T_{\rm ex} \sim 12$ K with small variation across the source. N_2D^+ also shows moderate optical depths, with total opacities of a few toward the continuum peak, and excitation temperatures $T_{\rm ex} \sim 9$ K, slightly lower than found for NH_2D.

In N6, the peak line opacity and excitation for both N_2D^+ and NH_2D are offset to the northeast from the compact continuum peak N6-mm, matching the offset seen in the integrated intensity maps. In contrast with SM1N, we also find higher excitation temperatures overall for N_2D^+ than NH_2D, with a maximum $T_{\rm ex} \sim 12$ K for N_2D^+. Measured $T_{\rm ex}$ values toward N6 agree well with N_2D^+ 3–2 observations at $\gtrsim$300 au resolution ($T_{\rm ex} \sim 10$ K; Bourke et al. 2012). While the values found are similar to or slightly less than previous estimates of the dust temperature at high spatial resolution in SM1N (Friesen et al. 2014), they are greater than predictions of the core dust temperature based on radiative transfer modeling of the expected radiation field in Oph A (Stamatellos et al. 2007). The lines thus originate in high-density gas where $n > n_{\rm crit}$ for each line, and constrain the gas (and dust) temperature at high densities within SM1N.

4.3. Molecular Column Densities

4.3.1. Ortho-H_2D^+

We determine the ortho-H_2D^+ column density from the Gaussian line fit. Following Vastel et al. (2006) and Friesen et al. (2014), we first determine the line opacity, τ, assuming an excitation temperature, $T_{\rm ex}$. We then determine the total column density, and estimate the partition function by reducing the H_2D^+ level structure to a two-level system as in Caselli et al. (2008). Both the line opacity and the partition function thus depend on our assumption for $T_{\rm ex}$. Friesen et al. (2014) assumed $T_{\rm ex} = 12$ K. As we will show further in Section 5, the best-fit density model for SM1N gives dust temperatures $T_d \sim 9$ K within several hundred au, in agreement with the excitation temperatures for N_2D^+ near the continuum peak ($T_{\rm ex} \sim 9$ K). Furthermore, at the high densities previously estimated for SM1N ($n \gtrsim 10^7$ K; Friesen et al. 2018), H_2D^+ should be very close to thermalized (Hugo et al. 2009). We thus assume $T_{\rm ex} = 10$ K for H_2D^+ in this analysis. We note that, given the line brightness, we obtain unphysical results for the line opacity if we assume $T_{\rm ex} \lesssim 9.5$ K.

Table 4
Line-fit Values for SM1N and N6

Par		SM1N			N6	
		oNH_2D	N_2D^+	H_2D^+	oNH_2D	N_2D^+
$\langle v_{LSR} \rangle$	(km s^{-1})	3.39 (0.03)	3.39 (0.03)	3.53 (0.07)	3.37 (0.5)	3.37 (0.4)
$\langle \sigma_v \rangle$	(km s^{-1})	0.14 (0.02)	0.15 (0.04)	0.27 (0.03)	0.11 (0.02)	0.09 (0.02)
$\langle T_{ex} \rangle$	(K)	12.2 (0.8)	8.0 (2.3)	10 (0)[a]	8.6 (2.4)	10.0 (1.9)
$\langle \tau \rangle$	⋯	10.8 (3.7)	3.1 (1.4)	0.9 (0.3)	6.6 (3.2)	5.4 (2.1)
$\langle N \rangle$	(cm^{-2})	$3.8(0.9) \times 10^{14}$	$2.0(0.8) \times 10^{12}$	$3.2\ (1.0) \times 10^{13}$	$1.6(0.7) \times 10^{14}$	$2.7(0.9) \times 10^{12}$
$\langle X \rangle$	⋯	$9.0(0.7) \times 10^{-10}$	$6.8(0.4) \times 10^{-12}$	$9.1(0.9) \times 10^{-11}$	$2.6(0.9) \times 10^{-9}$	$3.2(0.4) \times 10^{-11}$

Notes. The values in brackets are the standard deviation around the mean value reported.
[a] For H_2D^+, a constant T_{ex} was assumed; see text.

With $T_{ex} = 10$ K, we find a median line opacity $\tau = 0.9$, with a maximum $\tau = 1.8$. The median H_2D^+ column density is then $N(H_2D^+) = 3.2 \times 10^{13}$ cm^{-2}, with a maximum $N(H_2D^+) = 7.6 \times 10^{13}$ cm^{-2} that is offset by ∼0.″8 from the SM1N continuum peak. The maximum H_2D^+ column density is a factor of ∼6 greater than found in Friesen et al. (2014). This is partly due to the lower T_{ex} assumption in this work, and partly due to the improved sensitivity, in both line and spatial scale, of the newer data.

4.3.2. NH_2D and N_2D^+

For NH_2D and N_2D^+, where uncertainties in the fit T_{ex}, $\sigma_{Tex} < 3$ K, we use the fit parameters T_{ex}, τ, and σ_v to determine the total column density N of each species (Mangum & Shirley 2015):

$$N = \frac{8\pi\nu^3}{c^3}\frac{Q_{rot}}{g_u A_{ul}} \exp\left(\frac{E_u}{kT_{ex}}\right)\left[\exp\left(\frac{h\nu}{kT_{ex}}\right) - 1\right]^{-1} \int \tau dv. \quad (2)$$

Here, ν is the transition frequency, g_u is the degeneracy of the upper level, A_{ul} is the Einstein A coefficient, E_u is the energy of the upper level, and the integral of the opacity over the line width $\int \tau dv = \sqrt{2\pi}\,\sigma_v$.

For N_2D^+, we calculate the partition function $Q_{rot} = \sum_j g_j \exp(E_j/kT_{ex})$ over the first 10 energy levels, where the state degeneracy $g_j = 2J + 1$, given the fit T_{ex} at each pixel.

We determine $N(oNH_2D)$, rather than $N(NH_2D)$, as the ortho-to-para ratio is dependent on the physical conditions where the molecule is formed and can thus vary. Following Caselli et al. (2022), we take the values for E_u, g_u, and A_{ul} from the Leiden Atomic and Molecular Database (LAMDA; Schöier et al. 2005; van der Tak et al. 2020) and calculate the partition function up to the first 30 energy levels. We show the resulting column density maps across SM1N and N6 for all species in Figures 5 and 6, respectively. Note that the noisy appearance of the $N(NH_2D)$ map toward N6 is due to the high opacity of the line, where small variations in the T_{ex} and τ fits create jumps in the column density.

Toward SM1N, both $N(H_2D^+)$ and $N(N_2D^+)$ peak toward the continuum peak. N_2D^+ shows a second column density peak to the southeast of similar magnitude to that at the continuum peak, along the extension seen in the continuum. This second peak is also seen in the integrated intensity. In contrast, $N(NH_2D)$ shows less variation across the core, with slightly lower values at the continuum peak. Higher NH_2D column densities are found to the south of SM1N (seen as an integrated intensity peak in Figure 2). Toward N6, a clear drop in $N(N_2D^+)$ is seen toward N6-mm, and the greatest $N(oNH_2D)$ values are also offset from the compact source. For both N_2D^+ and NH_2D, the largest column densities are found northwest of the compact continuum source and coincident with the extended continuum emission. Additional regions of higher $N(N_2D^+)$ and $N(oNH_2D)$ extend to the southeast and northwest of the continuum.

5. Radiative Transfer Modeling of SM1N

We next analyze the radial density and temperature profiles of SM1N, using radiative transfer modeling to predict the continuum emission profile at the wavelengths observed with ALMA.

5.1. Radial Density Profiles

We create analytic density profiles following three different physically motivated models, and use the 3D Monte Carlo radiative transfer code RADMC-3D (Dullemond et al. 2012) to determine the radial temperature profile of the core, and the expected dust continuum flux density at each wavelength.[6] To simplify the problem, we assume a spherical model geometry and thus investigate radial density and temperature profiles only. While SM1N is elongated overall, this approach is reasonable given that the brightest emission at all wavelengths is centrally concentrated. In all but one case we assume the core is starless and include no internal heating source.

We investigate three types of radial density profiles. The first is a spherically symmetric Plummer model (Plummer 1911), which was first applied to starless cores by Whitworth & Ward-Thompson (2001). This centrally condensed density profile is constant with a value of n_0 inside some radius r_0, and then declines at $r > r_0$ following a power law with exponent $p/2$:

$$n(r) = \frac{n_0}{[1 + (r/r_0)^2]^{p/2}}. \quad (3)$$

This model is in agreement with single-dish observations which show that starless cores are centrally condensed, with a density profile that flattens at inner radii (e.g., Ward-Thompson et al. 1994; Alves et al. 2001; Tafalla et al. 2002).

Based on the observed properties of SM1N and previous analysis of the 1 mm continuum emission by Friesen et al. (2018), we modeled a set of density profiles with $n_0 = 10^6$–10^9 cm^{-3}, and transition radii $r_0 = 50$–300 au as inputs to the radiative transfer modeling. We set the outer power-law index $p = 2$, with the result that $n(r) \propto r^{-2}$ at large radii.

[6] https://www.ita.uni-heidelberg.de/~dullemond/software/radmc-3d/

The second radial density model is a singular power-law profile that follows

$$n = n_0 \left(\frac{r}{r_0} \right)^{-2}, \quad (4)$$

where n_0 is the gas density at radius r_0. This is the expected density profile for a SIS, and represents the envelopes of protostellar cores, where $n(r) \propto r^{-2}$ for all r (Larson 1969; Shu 1977). We choose a range of central densities such that the maximum density at 5 au is less than the density at which a FHSC would form ($n \sim 2 \times 10^{-11}$ cm^{-3}; Larson 1969).

Lastly, we test a broken power-law radial density profile that follows $n \propto r^{-2}$ at large radii, and is shallower inside some radius r_0 (but not flat, in contrast to the Plummer model). We again vary the central density n_0, and test a range of power-law exponents inside r_0, following

$$n = n_0 \left(\frac{r}{r_0} \right)^{-p}, \; r < r_0, \quad (5)$$

$$n = n_0 \left(\frac{r}{r_0} \right)^{-2}, \; r > r_0. \quad (6)$$

The physical motivation for this density profile is that predicted by a collapsing SIS. In Friesen et al. (2018), a simple, isothermal calculation suggested that the density profile of SM1N followed a broken power law, where in the inner part of the core $n(r) \propto r^{-1.3}$, transitioning to r^{-2} in the outer part at $r \gtrsim 200$ au. Here, we expand that analysis to model a broken power-law density profile self-consistently with the consequent dust temperature as a function of radius, and test several transition radii, 100 au $< r_0 <$ 300 au, and two inner power-law indices, $p = 1$ and $p = 1.5$, for the same range of n_0 as for the Plummer model above.

5.2. Dust Opacities and Radiation Sources

To model the dust temperature and emission, we use dust opacities based on the OH5 model from Ossenkopf & Henning (1994), for grains with thin ice mantles corresponding to a coagulation time $t = 10^5$ yr at density $n = 10^6$ cm^{-3}. We follow Svoboda et al. (2019) to extrapolate the dust opacities at wavelengths $\lambda < 1$ μm and $\lambda > 1.3$ mm. We include dust-scattering efficiencies and albedos based on Young & Evans (2005) and Weingartner & Draine (2001), respectively.

We assume that the cores are irradiated by an isotropic interstellar radiation field (ISRF). We use the ISRF model described by Black (1994), with the addition of the Draine (1978) description at ultraviolet wavelengths. We set the strength parameter, $G_0 = 1.7$. As stated above, however, Oph A and its embedded cores are also irradiated by the nearby star S1, which has a luminosity $L = 1100\,L_\odot$ (Bontemps et al. 2001) and an effective temperature $T = 16{,}000$ K. We model the expected flux of S1 as a function of wavelength as a blackbody at temperature T at the projected distance from SM1N.

The ALMA data resolve out emission on scales greater than $\sim 17''$ (Table 1). We therefore include dust opacity and scattering effects as a function of wavelength, applying the above dust absorption and scattering cross sections for a column density $N = 5 \times 10^{19}$ cm^{-2}, which corresponds to a density of $n \sim 10^3$ cm^{-3} over a distance of $\sim$0.01 pc, or roughly the thickness of the Oph A ridge. With these radiation field parameters, the dust temperatures at the core edges are $\sim$20–25 K for all density models, consistent with dust temperatures measured on larger scales (André et al. 1993; Santos et al. 2019) and dust temperature modeling of Oph A (Liseau et al. 2015).

For all models listed above, we assume the core is starless, and include no additional internal source of luminosity. We additionally create, however, a single model of a core with a power-law density profile as described above, where $n = 2 \times 10^{11}$ cm^{-3} at a radius of 5 au. At this density, the innermost regions of the core become optically thick, and the temperature rises until the thermal pressure supports the core against gravitational collapse (the FHSC). We add to this model an internal blackbody source of radius $r = 5$ au, mass $M = 0.05\,M_\odot$, and temperature $T = 170$ K, based on theoretical models of FHSCs (Larson 1969; Masunagaet al. 1998; Saigo et al. 2008). We note that FHSCs may have radii up to several tens of au in the case where the initial core is rapidly rotating, and the mass and temperature will both increase as the FHSC accretes more material from the infalling envelope.

5.3. Eliminating Models Based on Radial Temperature Profiles

For each density profile, the resulting radial temperature profile was determined via radiative transfer by RADMC-3D. The density and temperature profiles for a selection of parameters for the three classes of density profiles are shown in Figure 7.

Before simulating the ALMA observations, we further constrain the models by requiring the core temperatures to agree with measurements of the gas temperature in Oph A on both large and small spatial scales, and for predicted densities to match expected densities given the extent of the emission of the deuterated molecular lines. The initial models ensure dust temperatures are $\sim$20–25 K at the core edges, $\sim 10^4$ au. At scales $\sim$2500–4000 au, gas temperatures $T_K \sim$ 15–18 K based on NH_3 modeling (Friesen et al. 2009, 2018). Here, densities must be $n \gtrsim 10^3$ cm^{-3}, given the effective critical density of NH_3, and the gas and dust temperatures should be coupled. On the $\sim$100–2500 au scales sampled by our ALMA observations, the predicted dust temperatures must be consistent with the measured excitation temperature of the dense-gas tracers, $T_{ex} \gtrsim$ 8–9 K, based on the hyperfine N_2D^+ fits. These temperatures are slightly greater than typically assumed in isolated starless cores, where at the highest densities gas temperatures may become as low as $\sim$5–7 K (Crapsi et al. 2007; Pagani et al. 2007), due to the enhanced ISRF impacting Oph A. Pineda et al. (2022) find a similar result toward the core H-MM1, also in Ophiuchus, which they also ascribe to the strong radiation field. Densities must be $n \gtrsim 10^6$ cm^{-3} at radii of a few thousand au, given the critical densities of the N_2H^+ and N_2D^+ lines and their observed extents.

Examples of density and temperature profiles that match well the above requirements are shown in Figure 7. Overall, models with lower central densities show smaller drops in dust temperature toward the core interior (i.e., at small r). The radial temperature profiles are qualitatively similar for the Plummer and broken power-law density profiles, where models with higher central densities show sharp drops in T_d at the core edges, with a turnover to a more flat distribution at smaller core radii. The transition from steeply decreasing T_d to flatter T_d with r occurs at larger r for larger central n. Power-law density models show no such turnover in the relationship between T_d and r, and

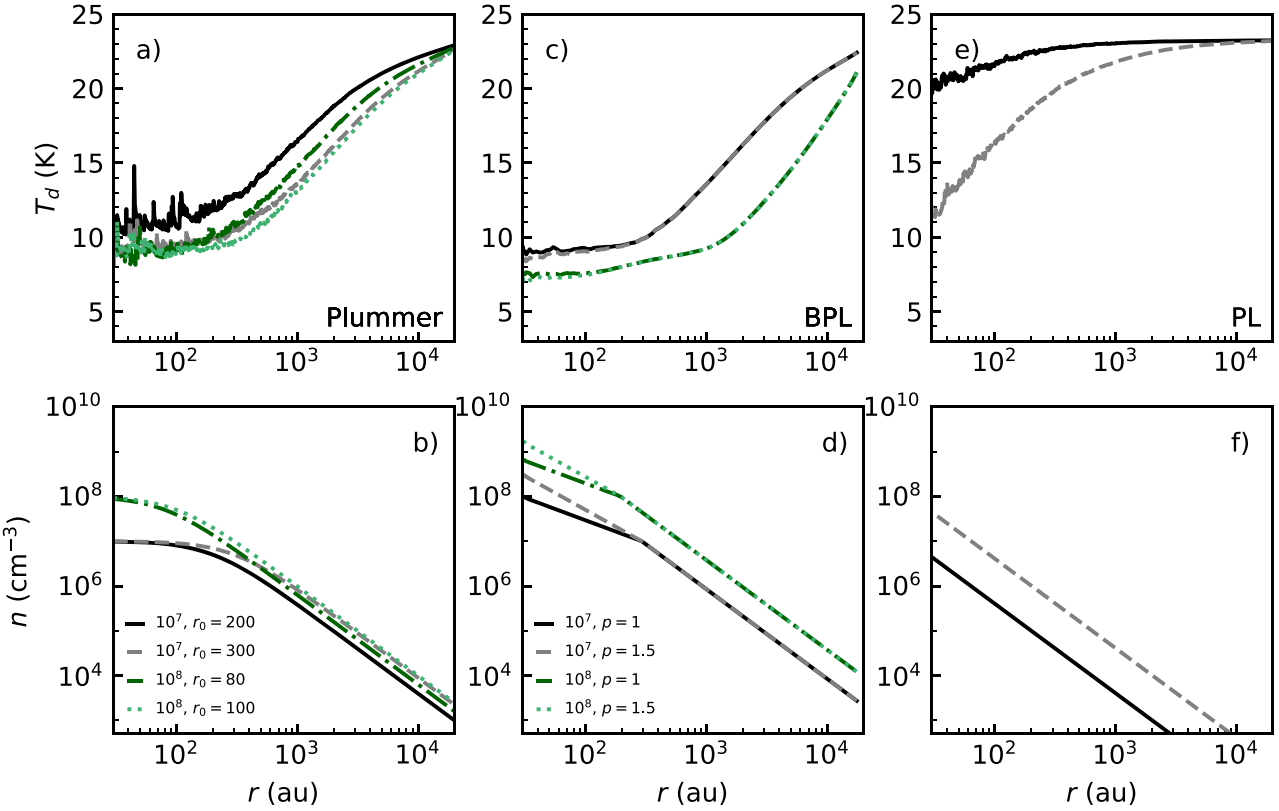

Figure 7. Here we show a selection of the core radial density models (bottom) and resulting radial temperature profiles (top) derived using RADMC-3D following the discussion in Section 5. The three columns show results from different radial density model families: the Plummer model (left), broken power law (BPL; middle), and power law (PL; right). Within each column linestyles and colors show different values of n_0, r_0, and p where varied. For the full range of parameters tested, see the text discussion. In the Plummer models, temperature spikes are due to photon packet limits and are not physical (and do not impact the final simulated images).

instead T_d consistently decreases toward smaller r, albeit more rapidly for models with higher central densities.

5.4. ALMA Simulations of Model Images

To compare directly the models with observations, synthetic images were made at 0.8 and 2 mm of each model that met the above requirements for dust temperature and overall density, and the cores were projected to a distance $d = 137.3$ pc.

We simulate ALMA observations of the predicted core emission that match the real integration and *uv* coverage achieved by the actual observations. We use the simulator toolkit within CASA to use the observed measurement sets at each wavelength to predict the observed visibilities for each model. At each wavelength, we predict the model visibilities for each ALMA configuration separately. We then combine the simulated measurement sets, applying a correction for the data weights when combining the 7 and 12 m measurement sets at 0.8 mm. We imaged the simulated data using `tclean` in CASA with the same parameters as were used for the observed data, with the exception of setting a fixed circular clean mask with a diameter of 8″, which is slightly smaller than the expected maximum angular scale achieved by the observations.

Figure 8 shows the observed continuum emission toward SM1N at 0.8 and 2 mm compared with the simulated emission maps at the same wavelengths that best fit the observed emission for each of the Plummer and broken power-law density profiles. Fit goodness is determined based on a comparison of the simulated and observed radial emission profiles, discussed further in Section 5.5. We furthermore show the simulated images of the model containing the warm blackbody source. We focus on the shorter-wavelength emission for this comparison, as no model reproduces well the observed 3 mm emission observed toward SM1N with ALMA.

A visual examination of the simulated observations shows clearly that only models with high central densities within a small central radius can match the actual core observations, particularly at longer wavelengths.

Comparing the simulated ALMA images for our simplistic FHSC model with more detailed simulations of FHSCs by Commerçon et al. (2012), we find that our predicted flux is a factor ∼2 greater than their simulations, which used a similar ALMA configuration. The authors show that the magnetic field strength influences the resulting expected flux densities of the formed FHSCs, but even their faintest, quasi-hydrostatic model predicts that a FHSC should be easily detected in our data as a compact source, given the depth of our 3 mm observations.

5.5. Observed and Simulated Radial Emission Profiles

We next compare directly the radial emission profiles of the model starless cores at the observed wavelengths with the ALMA data. We show in Figure 9 the radial profile of the observed emission toward SM1N at 0.8, 2, and 3 mm, centered on the peak emission location at 0.8 mm (Band 7), and averaged over radial annuli of 3 pixels, or ∼0.″3. We create similar radial emission profiles from the simulated emission maps for each model. We calculate the reduced chi square χ^2 between the model and the observations at each observed wavelength. We limit the calculation to within 5″ ($\lesssim$700 au), where we are

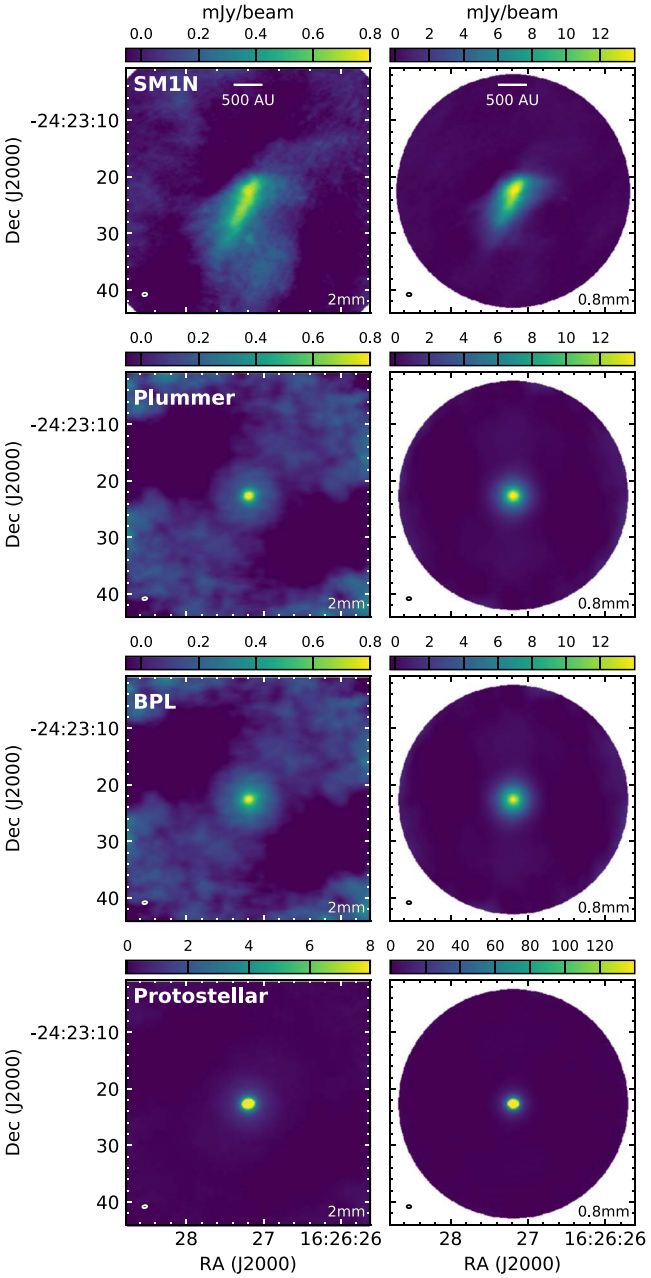

Figure 8. Comparison of the observed (top) and simulated (second to third rows) ALMA images at 2 mm (left) and 0.8 mm (right) of SM1N for the best-fit starless core models following the Plummer and broken power-law density profiles. In these rows the color scale is set to match the observations. The bottom row shows the power-law density profile model with an internal blackbody radiation source as described in Section 5.4, but the color scale extends a factor of 10 in flux density beyond the other rows.

comparing primarily the models against the compact central emission observed toward SM1N and omitting the outer, extended regions where our spherically symmetric model is not expected to agree well with observations.

We show in Figure 9 the observed radial emission profiles at 3, 2, and 0.8 mm toward SM1N (black and gray lines), along with predictions from the best-fit broken power-law and Plummer density models. We note that while we show the observed 3 mm radial emission profile, no model fits the observations well at this wavelength while matching emission profiles at the shorter wavelengths. As stated previously, this is likely due to the slightly

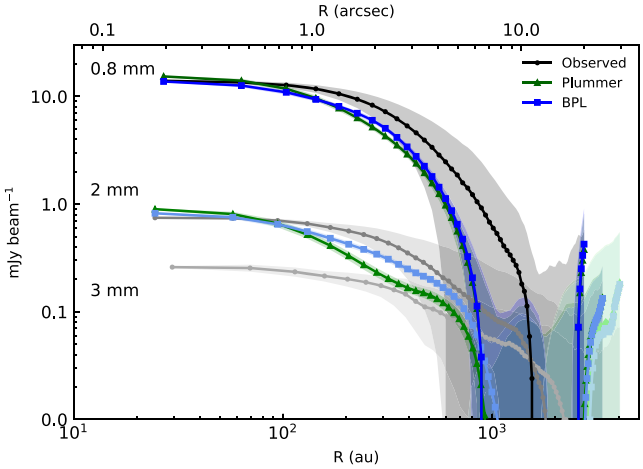

Figure 9. The observed radial emission profile toward SM1N at all observed ALMA wavelengths (black and gray lines and data points; the brightest emission is at 0.8 mm, followed by 2 mm and then 3 mm). Blue and green curves show the predicted radial emission profiles for the best-fit broken power-law (BPL) and Plummer density models, respectively. For all curves, shaded regions show the dispersion in flux values at that annulus band. As noted in Section 5.4, neither best-fit model predicts sufficient flux at 3 mm, and the predicted flux is below the limits of this plot.

greater sensitivity to larger-scale structures in the 3 mm observations, including the extended Oph A ridge, which is not included in our simple core model. Another possible reason for this discrepancy, however, could be a mismatch between the dust properties assumed in our modeling, particularly the assumption of an MRN dust size distribution (Mathis et al. 1977). If dust grains were able to grow in size within SM1N, we might expect to see elevated emission at 3 mm due to the impact of grain growth on the dust spectral index, β (as introduced in Section 3.2). Grain growth would lower the dust spectral index below the $\beta = 1.7$ value used here. Dust spectral indices have been observed to decrease in protostellar cores ($\beta \sim 1$) relative to starless cores ($\beta \sim 2$; Bracco et al. 2017), while models of observed dust emission require grain growth in the inner ~2000 au of the isolated starless core L1544 (Chacón-Tanarro et al. 2019). A comparison of the peak flux between 2 and 0.8 mm is consistent with $\beta \sim 1.7$–2.3, assuming $T_d \sim 10$ K, however making grain growth on several hundred au scales unlikely to be the cause of the discrepancy.

Considering only the shorter-wavelength emission, the best-fit density model is a broken power-law model with an inner radius $r_0 = 300$ au, a transition density $n_0 = 10^7$ cm^{-3} at r_0, and a power-law exponent $p = 1.0$ inside r_0. A slightly steeper $p = 1.5$ also fits well the 0.8 mm radial profile, but fits the 2 mm profile less well than the $p = 1.0$ model. Overall, the Plummer models agree less well with the observed data, with the best-fit model having $r_0 = 80$ au, and a slightly higher central density $n_0 = 10^8$ cm^{-3} compared with the best-fit broken power-law models. The set of models with single power-law density profiles were consistently poorer fits to the data than those with a turnover in n, and none fit the observations well. We thus do not show their simulated images or radial profiles here.

In the best-fitting models to the observed 0.8 and 2 mm emission, the dust temperature reaches a minimum of ~9–10 K within several hundred to ~1000 au (see Figure 7). Within ~500 au, the enclosed mass for both models is $M_{\rm enc} = 0.02\ M_\odot$, in agreement with previous mass calculations for SM1N from ALMA data at 1 and 0.8 mm that gave $M \sim 0.02$–$0.03\ M_\odot$

(Friesen et al. 2014, 2018) within ~500 au. The enclosed mass within 3×10^3 au is $M_{\rm enc} = 0.21\ M_\odot$ (broken power law) and $M_{\rm enc} = 0.18\ M_\odot$ (Plummer). This is less than the total core mass for SM1N, $M \sim 1.3\ M_\odot$, as determined from single-dish continuum data (Motte et al. 1998). This is not surprising, however, as we resolve out emission on scales $\gtrsim$2400 au that would add to the overall core mass. The density profile should be considered accurate on scales less than this.

6. Discussion

6.1. SM1N: Comparison with Core-collapse Models

The density model that best fits the observed radial emission profiles at 0.8 and 2 mm toward SM1N is a broken power-law model with an inner radius $r_0 = 300$ au, a density $n_0 = 10^7$ cm^{-3} at r_0, and a power-law exponent $p = 1.0$ inside r_0. At this density, the free-fall time is only a few $\times\ 10^3$ yr. Here, we compare SM1N's radial density profile and observed kinematics with predictions from several core-collapse models. We note that typical collapse models describe the evolution of a core in isolation, whereas SM1N exists within the Oph A ridge. In cluster-forming regions like Oph A, dense cores are typically more compact than cores found in more isolated environments (Ward-Thompson et al. 1999), and are more likely to be affected by, for example, protostellar feedback from nearby forming young stellar objects. SM1N is thus an example of the initial conditions of core collapse in a clustered environment, and may not be perfectly represented by the isolated collapse models described here; however, clustered collapse models in similar detail are not yet available.

A density profile $n \propto r^{-1}$, transitioning to $n \propto r^{-2}$, is similar to the predicted density profile of an SIS after collapse has begun, where $n \propto r^{-3/2}$ in the central region $r < r_0$ undergoing free-fall collapse (Shu 1977). The transition radius moves outward as the collapse proceeds ("inside-out" collapse). In this model, however, an accreting source has already formed at the center of the cloud, whereas our modeling of the continuum emission and analysis of the molecular-line data shows no significant source of luminosity can exist within SM1N.

The density model is also similar to that predicted for a gravitationally contracting, unstable BES. Here, the inner radius describes the transition between a flat inner-density profile and the steep-outer density profile, and is equal to the Jeans length given by the sound speed and central density (Keto & Caselli 2010), as we find in our best-fit density model. Over time, the inner region increases in density and decreases in radius, such that the outer, singular density profile dominates more of the core and the density profile approaches that of the SIS. This contraction predates the formation of an accreting source. This model was found to fit the more isolated starless core L1544 (with a lower central density $n_c = 10^7$ cm^{-3}; Keto et al. 2015). The broken power-law model continues to increase in density as $r \to 0$, however, in contrast to the BES model. If we require a flatter density profile for SM1N inside of the transition region to better match a BES, as in the Plummer model, we find that the best-fit model has a central density $n_c = 10^8$ cm^{-3} and a transition radius of only 80 au, less than the Jeans length by a factor of 3 and thus smaller than predicted from these quasi-static evolutionary models.

Gómez et al. (2021) model core collapse in a constant-density environment, such that the collapsing core continues to accrete from its surroundings. Such a model may be more applicable to cores within a dense molecular filament or ridge like Oph A. This global-gravitational-collapse model predicts a similar density profile, where $p < 2$ at earlier stages of collapse, and the inner Jeans-stable region shrinks over time as the density increases to eventually match an SIS-type density profile at the time of protostar formation.

The evolution of a collapsing BES predicts that the infall velocity, v_{in}, is linear with r to near r_0, and then decreases with increasing r (Foster & Chevalier 1993). Similarly, Gómez et al. (2021) show that for $p \leqslant 2$ in the global-gravitational-collapse model, infall speeds should also decrease toward the core center. In a scale-free model of free-fall gravitational collapse, Li (2018) find that $v_{ff} = -f\sqrt{GM(r)/r}$, where $M(r)$ is the mass internal to some radius r, and f is a constant that depends on the scale of turbulence driving. Post-protostar formation, the SIS model predicts v_{in} increases as $r^{-1/2}$.

Since H_2D^+ and N_2D^+ are largely optically thin, any infall motion will present as increased line widths. In the collapsing BES model, Keto & Caselli (2010) predict that the line FWHM for N_2H^+ (1–0) reaches ~0.35 km s^{-1} when $n_c = 10^8$ cm^{-3}, giving a nonthermal velocity dispersion $\sigma_{\rm NT} = 0.15$ km s^{-1} at $T = 5$ K. Toward SM1N, velocity dispersions σ_v for H_2D^+ and N_2D^+ appear to increase near the continuum peak, with smaller values found at the core edges (Figure 5). We show in Figure 10 the radial profiles of $\sigma_{\rm NT}$ for H_2D^+, N_2D^+, and NH_2D. The nonthermal velocity dispersion was calculated assuming a constant gas temperature of 10 K. For H_2D^+, we additionally determine the intrinsic velocity dispersion given the optical depth of the line following Hacar et al. (2016) prior to calculating $\sigma_{\rm NT}$. For H_2D^+ and N_2D^+, $\sigma_{\rm NT}$ is essentially constant to $r \sim 200$ au, and then decreases at larger radii, albeit with larger scatter due to sensitivity and the appearance of a second N_2D^+ emission peak toward SM1N. In particular, $\sigma_{\rm NT} \sim 0.15$ km s^{-1} for N_2D^+, and slightly greater for H_2D^+.

Figure 10 furthermore highlights a trend of increased $\sigma_{\rm NT}$ from NH_2D through N_2D^+ to H_2D^+. NH_2D has a lower effective critical density than N_2D^+ and H_2D^+, however. We thus find a potential increase in $\sigma_{\rm NT}$ with increasing density in the core, assuming a constant gas temperature and that NH_2D, N_2D^+, and H_2D^+ trace progressively denser gas. This may be in conflict with the collapsing BES model, as infall speeds should become smaller interior to the transition radius, where densities are higher. If, however, NH_2D traces gas outside the transition radius, then the observations are not in conflict with the model.

To examine further how well the different molecules may trace the highest-density gas, we show in Figure 10 (bottom) the radially averaged column densities of the three molecular species toward SM1N, centered on the continuum peak and normalized to the value at $r = 1''$. As expected from the column density maps, both $N(H_2D^+)$ and $N(N_2D^+)$ peak with the continuum, while $N(\mathrm{o}NH_2D)$ decreases by a factor ~30% compared with its highest value within $\gtrsim$100 au of the continuum peak. The NH_2D abundance relative to H_2 thus also decreases toward the continuum peak.

Given the projected $N(H_2)$ as a function of radius from the best-fitting density model for SM1N, we find roughly constant radial H_2D^+ and N_2D^+ abundances toward SM1N within several hundred au, where the mean $X(H_2D^+) = 9.1 \times 10^{-11}$ and $X(N_2D^+) = 6.8 \times 10^{-12}$. The mean $X(NH_2D) = 9 \times 10^{-10}$, and decreases slightly at the continuum peak. The $N(NH_2D)$ and $X(NH_2D)$ profiles suggest that NH_2D (and consequently NH_3) are depleted from the gas phase via freeze-

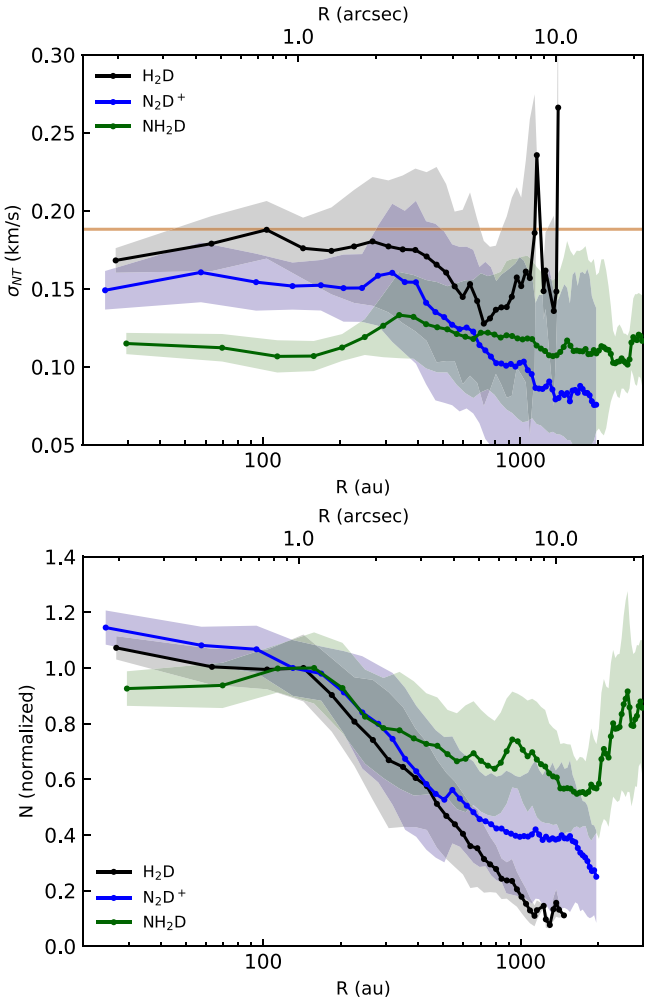

Figure 10. Top: radial σ_{NT} profiles toward SM1N from Gaussian (H_2D^+) and hyperfine (N_2D^+, NH_2D) fits to the emission lines, centered on the continuum peak location. The shaded areas show the 1σ standard deviation around the mean value. The red line shows the sound speed at 10 K. The nonthermal component of the velocity dispersion is subsonic for all lines, and appears to increase toward higher densities given the molecular tracers used. Bottom: radial column density profiles of SM1N for H_2D^+, N_2D^+, and NH_2D, normalized to their value at $r = 1''$. Shaded areas show the 1σ dispersion around the mean value. The radial profiles are centered on the continuum peak. Toward SM1N, the peak $N(H_2D^+)$ and $N(N_2D^+)$ values are found near the continuum peak and are closely correlated, whereas $N(NH_2D)$ peaks are offset from the continuum.

out onto dust grains at the highest densities in the SM1N core. Similar results were found via chemical modeling of the evolved starless core L1544 (Caselli et al. 2022), as well as for the starless core H-MM1 (Pineda et al. 2022). In the case of L1544, the central density is slightly lower than found for SM1N, and the transition radius is significantly larger. This result is further evidence of the presence of a "complete depletion zone" within cores prior to the formation of a protostar (Walmsleyet al. 2004). Additional modeling of the chemistry as a function of radius may reveal whether N_2D^+ is also depleted at small scales in SM1N, but is beyond the scope of this paper. Regardless, given the apparent depletion of NH_2D, the smaller nonthermal gas motions traced by this line originate in regions with lower density, and σ_{NT} therefore increases with core density (but remains subsonic) in SM1N.

As noted above, this is not necessarily incompatible with the collapsing BES model, as long as the lower-density gas traced by NH_2D is outside of the transition radius where v_{in} begins to decrease with *increasing* radius. Our best-fit $r_0 \sim 80$–300 au for the broken power-law and Plummer models, respectively. This is similar to the radius where we see the drop in $N(NH_2D)$ in Figure 10, so our observations are consistent with the BES predictions. It is not clear whether the global-collapse model also predicts a turnover in v_{in}; if not, the kinematics of SM1N are not consistent with this model. We thus argue that the starless core SM1N is undergoing either inside-out gravitational collapse or is in a highly evolved, contracting BES state.

6.2. N6: Comparison with First Hydrostatic Core Predictions

What is the nature of the compact source N6-mm? We first want to rule out the serendipitous detection of a faint submillimeter galaxy (SMG) in our field of view. Tamura et al. (2015) argue that high-redshift SMGs can appear similar to FHSCs at millimeter wavelengths. Using the background source counts at 1.1 mm from Hatsukade et al. (2016), we estimate that we may detect ~0.3 sources per 1.1 mm field with flux densities similar or greater than that detected toward N6-mm. Deep radio searches with the Very Large Array, however, find no corresponding 6 cm source (Leous et al. 1991; Gagné et al. 2004). Chen et al. (2011) argue that a lack of radio detection implies that the SMG must be at much higher redshift than assumed by Hatsukade et al. (2016), $\bar{z} \sim 2.5$. In this case, we would expect a rising SED toward shorter wavelengths and a detection by Herschel or Spitzer, but no sources are detected toward N6-mm at these wavelengths. Furthermore, we detect extended continuum emission around N6-mm, and the distribution of H_2D^+, N_2D^+, and NH_2D avoid the continuum peak, suggesting that the dense gas is affected by N6-mm. We thus argue that it is very unlikely that N6-mm is a background, high-redshift SMG.

FHSC candidates are generally identified via compact continuum sources, coupled in some cases with the detection of low-velocity bipolar outflows, and either a lack of point-source emission at wavelengths shorter than ~160 μm or a very low luminosity $L_{bol} < 0.1\ L_\odot$ (e.g., Hirano & Liu 2014; Gerin et al. 2015). In some cases, compact continuum detections were not present in follow-up observations (e.g., Per-bolo 45 and L1448 IRS2E; Maureira et al. 2020), and these sources were ruled out as FHSC candidates. Fujishiro et al. (2020) identify a compact source, MC35-mm, in Taurus, with a tentative low-velocity (~2–4 km s^{-1}) bipolar outflow extending only a few $\times\ 10^3$ au, but at ~800 au resolution are not able to identify a point source similar to N6-mm.

In contrast to SM1N, the distribution of dense-gas tracers near N6-mm is suggestive of (very compact) heating by an embedded source. Any embedded source must have $L_{bol} < 0.1\ L_\odot$, the upper limit for a very-low-luminosity object (VeLLO), based on Herschel 70 μm data and following the tight relationship between 70 μm emission and L_{bol} for protostars (Dunham et al. 2008). Unfortunately, the 70 μm-bright Oph A ridge precludes a more stringent upper limit. The expected luminosity for a FHSC at 70 μm is ~200–300 mJy at the distance to Ophiuchus (Boss & Yorke 1995; Masunagaet al. 1998; Enoch et al. 2010), just below the observable 70 μm limit near N6-mm. N6-mm is also fainter than predictions for FHSCs at longer wavelengths. Enoch et al. (2010) model the SED of FHSC candidate Per-Bolo 58, finding a good fit with a source with $L = 0.012\ L_\odot$ and $T_{bol} = 100$ K within $R = 1.7$ au. At 850 μm (0.85 mm), the flux density of Per-Bolo 58 is 920 mJy, however,

nearly 2 orders of magnitude greater than N6-mm (11 mJy), and Maureira et al. (2020) argue that this source is in fact a Class 0 protostar. Indeed, the observed flux density at 0.8 mm toward N6-mm is much less than predicted by simulated ALMA observations of FHSC models, unless we are viewing N6-mm nearly edge-on through a forming disk or pseudo-disk structure (Commerçon et al. 2012). In this case, the 0.8 mm emission would be optically thick, obscuring the embedded FHSC. This possibility seems unlikely, however, as the observed dust spectral index is consistent with typical ISM values, rather than the shallower slope expected for high optical depth (although deeper observations at 1.1 mm would constrain this better, as described in Section 3.2).

Similar to arguments used to constrain the temperature and density structure for SM1N, N_2D^+ and NH_2D both show high T_{ex} values that indicate that the line emission originates from gas with temperatures $\gtrsim$9–10 K, and densities $n \gtrsim 10^5$–10^6 cm^{-3}. In contrast to SM1N, however, we find slightly larger NH_2D σ_{NT} values compared with N_2D^+, with typical values σ_{NT} ~0.09 and σ_{NT} ~0.07 km s^{-1}, respectively, such that the nonthermal component of the velocity dispersion decreases rather than increases toward higher densities. Furthermore, we do not detect compact significant H_2D^+ emission toward N6-mm or the extended continuum structure, implying that H_2D^+ is depleted in the gas phase. This may be due to a further deuterium fractionation from H_3^+ and H_2D^+ toward D_2H^+ and D_3^+. Alternatively, gas temperatures may be enhanced toward N6-mm such that the backwards direction of the H_2D^+-formation reaction is again allowed to occur, destroying H_2D^+ and consequently N_2D^+ and NH_2D. As noted in Section 3.2, single-dish temperature measurements toward N6 are warmer than in isolated starless cores, with T_K ~ 15–20 K. Only a small increment in temperature due to an embedded, warm object would thus be needed to allow for the decrease in H_2D^+ (and hence N_2D^+ and NH_2D) abundance. Aikawa et al. (2008) show that the CO sublimation radius, where $T \gtrsim 20$ K, is only ~100 au at the time of protostar formation, similar to the resolution of our ALMA observations. Deuterium fractionations can remain high in the envelopes of young protostellar sources (Giers et al. 2023), in agreement with the observed N_2D^+ and NH_2D within N6 (but offset from N6-mm).

The typical mass of a FHSC is $M \sim 0.05$ $M_\odot$ (Boss & Myhill 1992; Masunagaet al. 1998), but can be lower in, for example, weakly magnetized cores (Commerçon et al. 2012). If the continuum emission is optically thin, we calculate a mass $M = 0.0015$ $M_\odot$ (1.6 M_{Jup}) in the compact source, giving an average $n \sim 3 \times 10^6$ cm^{-3}, embedded within extended emission with mass $M \sim 0.01$–0.02 $M_\odot$ (Section 3.2). N6-mm could thus potentially be a FHSC if the continuum emission is optically thick, or alternately a proto-brown dwarf. Its final mass will depend on how efficiently it can accrete mass from the larger core ($M = 0.29$ $M_\odot$; Bourke et al. 2012). Assuming a ~30% mass accretion efficiency (Alves et al. 2007), the final source mass would fall on the border between a brown dwarf and stellar object. The N6-mm mass and luminosity upper limit are similar to values found for proto- or Class 0 brown dwarfs identified in Lupus (Santamaría-Miranda et al. 2021).

Outflows have been detected toward brown-dwarf candidates (Kim et al. 2019), in some cases with extents of ~10″–20″. FHSCs have been predicted to drive compact (~hundreds of au), low-velocity (~1–4 km s^{-1}) outflows (Commerçon et al. 2012; Hincelin et al. 2016), where the values depend on the magnetization of the contracting core. Outflow searches toward N6 are challenging due to the presence of the VLA 1623 outflow to the southwest of the N6 core, but previous studies would have been sensitive to outflows on $\gtrsim$10″ scales. Friesen et al. (2018) identify a potential compact, low-velocity red outflow lobe in CO emission to the northeast of N6-mm. Young et al. (2019) argue, however, that any outflows from FHSCs would be too compact and low-mass to be detectable in emission like CO with ALMA, ruling out a number of FHSC candidates in the literature, including promising candidates L1451-mm (Maureira et al. 2020; Wakelam et al. 2022) and Barnard 1b-N and 1b-S (Young et al. 2019). The upper L_{bol} limit shows that, at most, N6-mm may be a VeLLO, while the lack of large-scale outflows limits the dynamical age of any embedded, accreting source to $\lesssim 10^3$ yr. Thus, N6-mm remains one of the best FHSC candidates yet identified.

6.3. On the Frequency of Compact Structures in Oph A

Previous surveys to detect compact structure in starless cores at high resolution have detected between zero and a few objects out of tens of targets (Dunham et al. 2016; Kirk et al. 2017). At somewhat lower resolution than this study (900 au spatial resolution), Tokuda et al. (2020) identify compact emission toward a third of prestellar targets in the Taurus molecular cloud, and argue that the lifetime of prestellar cores approaches the free-fall time as the core density increases. This implies that it should be unlikely to detect two objects like SM1N and N6-mm at these transitional stages, with only ~10^3–10^4 yr timescales, in such a small region as Oph A. Indeed, Oph A also contains several protostellar sources discovered with ALMA observations that remain undetected at shorter wavelengths (Friesen et al. 2014, 2018; Kawabe et al. 2018), implying at least six low-mass stars have formed or are in the process of forming within the expected Class 0 lifetime of ~0.1–0.16 Myr (Evans et al. 2009).

As noted previously, Oph A is a dense ridge within a clustered star-forming environment. Dust and gas temperatures are greater than in typical cores in more isolated environments due to heating by nearby stars (Liseau et al. 2015; Chen & Hirano 2018). For example, Oph A lies between two B-type stars, S1 and HD 147889, resulting in known photodissociation regions (PDRs) along both the western and eastern edges (e.g., Liseau et al. 1999; Kamegai et al. 2003), although there does not seem to be a strong pressure gradient at the PDR border (Larsson & Liseau 2017). More generally, it has been argued that the morphology of L1688 may be explained by external compression from the Sco OB2 association (Loren & Wootten 1986). Furthermore, there is evidence for multiple outflows from nearby protostars, including the extended VLA 1623 outflow (Nakamura et al. 2011), that may impinge on the dense gas itself. Oph A and its embedded sources are thus evolving in a dynamic environment, which may be expected to produce a burst of star formation activity within a shorter time period than in isolated environments. Such a burst would produce more objects in a dynamically evolved state than expected for models of, for example, constant star formation.

7. Summary

Here, we have investigated in detail continuum emission and dense-gas-tracing molecular-line emission at ~100 au resolution toward the previously identified SM1N and N6-mm sources in

Ophiuchus A. We have also identified another compact continuum source within the larger Oph A ridge, which we label N6-w. The continuum SED and measured fluxes for N6-w are consistent with previously detected protostellar sources in Oph A, but additional, targeted continuum and line observations are needed to confirm its classification.

Previous analyses of observational data have consistently confirmed the starless nature of SM1N, despite its centrally peaked density profile and subsequent apparent instability to gravitational collapse. Here, we have tested a range of radial density profiles, determining via radiative transfer analysis their resulting radial temperature profiles, and predicted emission as observed by ALMA. Our results show that SM1N cannot contain a low-luminosity protostar. The predicted emission for theoretical FHSC models are also bright compared with the ALMA-detected emission from SM1N, even if the FHSC is only $\sim$5 au in radius (compared with our resolution of $\sim$100 au). We thus conclude that SM1N remains starless, but in a highly unstable dynamical state.

The observed emission from the dense-gas tracers, H_2D^+, N_2D^+, and NH_2D, are consistent with this conclusion via the dust continuum analysis. Both H_2D^+ and N_2D^+ emission peaks are coincident with the continuum peak, with no evidence of decreasing abundance as would be expected if a warm region existed at small radii around a FHSC or young protostar. We show that NH_2D is likely depleted toward the core center due to freeze-out onto dust grains, rather than by destruction via heating and CO release. The velocity dispersions at small radii ($\lesssim$300 au) are relatively constant, with nonthermal motions similar to the sound speed at 10 K. We find a potential increase in σ_{NT} with increasing density in the core, assuming a constant gas temperature and that NH_2D, N_2D^+, and H_2D^+ trace progressively denser gas. This increase of nonthermal width with increasing density is consistent with SM1N being in a state of dynamic collapse right before the formation of a central protostellar system.

Toward N6, we confirm the presence of a compact continuum source, N6-mm, within the core (Friesen et al. 2018). In contrast to starless SM1N, however, the dense-gas tracers avoid the continuum peak, consistent with the presence of an embedded source warming the immediate surroundings but retaining high deuterium fractions in the envelope. The estimated mass, assuming optically thin dust emission, is less than predicted for a FHSC, and its (sub)millimeter flux is similarly low compared with FHSC models. The measurements are consistent with several proto-brown-dwarf candidates. We do not detect an increase in the velocity dispersion with increasing density toward N6, and instead NH_2D σ_{NT} values are slightly greater than those measured for N_2D^+, although for both species σ_{NT} remains subsonic. The lack of detected outflows indicates that the dynamical age of a potential embedded, accreting source is $\lesssim 10^3$ yr.

For both sources, additional modeling of the expected molecular abundances and kinematics would provide further tests of prestellar core infall models.

Acknowledgments

We thank the anonymous referee for the feedback and comments that improved the manuscript. This paper makes use of the following ALMA data: ADS/JAO.ALMA# 2018.1.00935.S, ADS/JAO.ALMA# 2017.1.01006.S, and ADS/JAO.ALMA# 2013.1.00937.S. ALMA is a partnership of ESO (representing its member states), NSF (USA), and NINS (Japan), together with NRC (Canada) and NSC and ASIAA (Taiwan), in cooperation with the Republic of Chile. The Joint ALMA Observatory is operated by ESO, AUI/NRAO, and NAOJ. The University of Toronto operates on the traditional land of the Huron-Wendat, the Seneca, and, most recently, the Mississaugas of Credit River; we are grateful to have the opportunity to work on this land. Z.Y.L. is supported in part by NASA grant No. 80NSSC20K0533 and NSF grant AST-1910106.

Continuum maps, data cubes, and integrated intensity maps are publicly available at the CADC via the following link: doi:10.11570/23.0017.

Facility: ALMA.

Software: CASA (CASA Team et al. 2022), RADMC-3D (Dullemond et al. 2012), astropy (Astropy Collaboration et al. 2013, 2018, 2022).

ORCID iDs

Rachel K. Friesen https://orcid.org/0000-0001-7594-8128
Tyler L. Bourke https://orcid.org/0000-0001-7491-0048
Paola Caselli https://orcid.org/0000-0003-1481-7911
James Di Francesco https://orcid.org/0000-0002-9289-2450
Zhi-Yun Li https://orcid.org/0000-0002-7402-6487
Jaime E. Pineda https://orcid.org/0000-0002-3972-1978

References

Aikawa, Y., Wakelam, V., Garrod, R. T., & Herbst, E. 2008, ApJ, 674, 984
Alves, J., Lombardi, M., & Lada, C. J. 2007, A&A, 462, L17
Alves, J. F., Lada, C. J., & Lada, E. A. 2001, Natur, 409, 159
Andersen, B. C., Stephens, I. W., Dunham, M. M., et al. 2019, ApJ, 873, 54
André, P., Martin-Pintado, J., Despois, D., & Montmerle, T. 1990, A&A, 236, 180
André, P., Ward-Thompson, D., & Barsony, M. 1993, ApJ, 406, 122
Astropy Collaboration, Price-Whelan, A. M., Lim, P. L., et al. 2022, ApJ, 935, 167
Astropy Collaboration, Price-Whelan, A. M., Sipőcz, B. M., et al. 2018, AJ, 156, 123
Astropy Collaboration, Robitaille, T. P., Tollerud, E. J., et al. 2013, A&A, 558, A33
Bacmann, A., André, P., Puget, J. L., et al. 2000, A&A, 361, 555
Bergin, E. A., & Tafalla, M. 2007, ARA&A, 45, 339
Black, J. H. 1994, in ASP Conf. Ser. 58, Energy Budgets of Diffuse Clouds, ed. R. M. Cutri & W. B. Latter (San Francisco, CA: ASP), 355
Bontemps, S., André, P., Kaas, A. A., et al. 2001, A&A, 372, 173
Boss, A. P., & Myhill, E. A. 1992, ApJS, 83, 311
Boss, A. P., & Yorke, H. W. 1995, ApJL, 439, L55
Bourke, T. L., Myers, P. C., Caselli, P., et al. 2012, ApJ, 745, 117
Bracco, A., Palmeirim, P., André, P., et al. 2017, A&A, 604, A52
CASA Team, Bean, B., Bhatnagar, S., et al. 2022, PASP, 134, 114501
Caselli, P., Pineda, J. E., Sipilä, O., et al. 2022, ApJ, 929, 13
Caselli, P., Pineda, J. E., Zhao, B., et al. 2019, ApJ, 874, 89
Caselli, P., Vastel, C., Ceccarelli, C., et al. 2008, A&A, 492, 703
Chacón-Tanarro, A., Pineda, J. E., Caselli, P., et al. 2019, A&A, 623, A118
Chen, C.-C., Cowie, L. L., Wang, W.-H., Barger, A. J., & Williams, J. P. 2011, ApJ, 733, 64
Chen, Y.-C., & Hirano, N. 2018, ApJ, 868, 80
Commerçon, B., Levrier, F., Maury, A. J., Henning, T., & Launhardt, R. 2012, A&A, 548, A39
Crapsi, A., Caselli, P., Walmsley, M. C., & Tafalla, M. 2007, A&A, 470, 221
Daniel, F., Coudert, L. H., Punanova, A., et al. 2016, A&A, 586, L4
Daniel, F., Faure, A., Wiesenfeld, L., et al. 2014, MNRAS, 444, 2544
Di Francesco, J., André, P., & Myers, P. C. 2004, ApJ, 617, 425
Draine, B. T. 1978, ApJS, 36, 595
Dullemond, C. P., Juhasz, A., Pohl, A., et al. 2012, RADMC-3D: A multi-purpose radiative transfer tool, Astrophysics Source Code Library, ascl:1202.015
Dunham, M. M., Crapsi, A., Evans, N. J., II., et al. 2008, ApJS, 179, 249
Dunham, M. M., Offner, S. S. R., Pineda, J. E., et al. 2016, ApJ, 823, 160
Enoch, M. L., Corder, S., Duchêne, G., et al. 2011, ApJS, 195, 21

Enoch, M. L., Evans, N. J., II., Sargent, A. I., & Glenn, J. 2009, ApJ, 692, 973
Enoch, M. L., Lee, J.-E., Harvey, P., Dunham, M. M., & Schnee, S. 2010, ApJL, 722, L33
Evans, N. J., Dunham, M. M., Jørgensen, J. K., et al. 2009, ApJS, 181, 321
Foster, P. N., & Chevalier, R. A. 1993, ApJ, 416, 303
Friesen, R. K., Di Francesco, J., Bourke, T. L., et al. 2014, ApJ, 797, 27
Friesen, R. K., Di Francesco, J., Shirley, Y. L., & Myers, P. C. 2009, ApJ, 697, 1457
Friesen, R. K., Pon, A., Bourke, T. L., et al. 2018, ApJ, 869, 158
Fujishiro, K., Tokuda, K., Tachihara, K., et al. 2020, ApJL, 899, L10
Gagné, M., Skinner, S. L., & Daniel, K. J. 2004, ApJ, 613, 393
Gerin, M., Pety, J., Fuente, A., et al. 2015, A&A, 577, L2
Giers, K., Spezzano, S., Caselli, P., et al. 2023, A&A, 676, A78
Ginsburg, A., & Mirocha, J. 2011, pyspeckit: Python Spectroscopic Toolkit, Astrophysics Source Code Library, ascl:1109.001
Ginsburg, A., Sokolov, V., de Val-Borro, M., et al. 2022, AJ, 163, 291
Gómez, G. C., Vázquez-Semadeni, E., & Palau, A. 2021, MNRAS, 502, 4963
Greene, T. P., & Young, E. T. 1992, ApJ, 395, 516
Hacar, A., Alves, J., Burkert, A., & Goldsmith, P. 2016, A&A, 591, A104
Hatsukade, B., Kohno, K., Umehata, H., et al. 2016, PASJ, 68, 36
Hincelin, U., Commerçon, B., Wakelam, V., et al. 2016, ApJ, 822, 12
Hirano, N., & Liu, F.-c. 2014, ApJ, 789, 50
Hugo, E., Asvany, O., & Schlemmer, S. 2009, JChPh, 130, 164302
Jørgensen, J. K., van Dishoeck, E. F., Visser, R., et al. 2009, A&A, 507, 861
Kamegai, K., Ikeda, M., Maezawa, H., et al. 2003, ApJ, 589, 378
Kawabe, R., Hara, C., Nakamura, F., et al. 2018, ApJ, 866, 141
Kepley, A. A., Tsutsumi, T., Brogan, C. L., et al. 2020, PASP, 132, 024505
Keto, E., & Caselli, P. 2010, MNRAS, 402, 1625
Keto, E., Caselli, P., & Rawlings, J. 2015, MNRAS, 446, 3731
Kim, G., Lee, C. W., Maheswar, G., et al. 2019, ApJS, 240, 18
Kirk, H., Dunham, M. M., Di Francesco, J., et al. 2017, ApJ, 838, 114
Larson, R. B. 1969, MNRAS, 145, 271
Larsson, B., & Liseau, R. 2017, A&A, 608, A133
Leous, J. A., Feigelson, E. D., Andre, P., & Montmerle, T. 1991, ApJ, 379, 683
Li, G.-X. 2018, MNRAS, 477, 4951
Liseau, R., Larsson, B., Lunttila, T., et al. 2015, A&A, 578, A131
Liseau, R., White, G. J., Larsson, B., et al. 1999, A&A, 344, 342
Loren, R. B., & Wootten, A. 1986, ApJ, 306, 142
Mangum, J. G., & Shirley, Y. L. 2015, PASP, 127, 266
Masunaga, H., Miyama, S. M., & Inutsuka, S.-i. 1998, ApJ, 495, 346
Mathis, J. S., Rumpl, W., & Nordsieck, K. H. 1977, ApJ, 217, 425
Maureira, M. J., Arce, H. G., Dunham, M. M., et al. 2020, MNRAS, 499, 4394
Motte, F., Andre, P., & Neri, R. 1998, A&A, 336, 150
Nakamura, F., Kamada, Y., Kamazaki, T., et al. 2011, ApJ, 726, 46
Ortiz-León, G. N., Loinard, L., Kounkel, M. A., et al. 2017, ApJ, 834, 141
Ossenkopf, V., & Henning, T. 1994, A&A, 291, 943
Pagani, L., Bacmann, A., Cabrit, S., & Vastel, C. 2007, A&A, 467, 179
Pineda, J. E., Arzoumanian, D., André, P., et al. 2023, in ASP Conf. Ser. 534, Protostars and Planets VII, ed. S. Inutsuka et al. (San Francisco, CA: ASP), 233
Pineda, J. E., Harju, J., Caselli, P., et al. 2022, AJ, 163, 294
Plummer, H. C. 1911, MNRAS, 71, 460
Pon, A., Plume, R., Friesen, R. K., et al. 2009, ApJ, 698, 1914
Redaelli, E., Bizzocchi, L., Caselli, P., et al. 2019, A&A, 629, A15
Roberts, H., & Millar, T. J. 2000, A&A, 364, 780
Saigo, K., Tomisaka, K., & Matsumoto, T. 2008, ApJ, 674, 997
Santamaría-Miranda, A., de Gregorio-Monsalvo, I., Plunkett, A. L., et al. 2021, A&A, 646, A10
Santos, F. P., Chuss, D. T., Dowell, C. D., et al. 2019, ApJ, 882, 113
Schöier, F. L., van der Tak, F. F. S., van Dishoeck, E. F., & Black, J. H. 2005, A&A, 432, 369
Shu, F. H. 1977, ApJ, 214, 488
Stamatellos, D., Whitworth, A. P., & Ward-Thompson, D. 2007, MNRAS, 379, 1390
Svoboda, B. E., Shirley, Y. L., Traficante, A., et al. 2019, ApJ, 886, 36
Tafalla, M., Myers, P. C., Caselli, P., Walmsley, C. M., & Comito, C. 2002, ApJ, 569, 815
Tamura, Y., Kawabe, R., Shimajiri, Y., et al. 2015, ApJ, 808, 121
Tokuda, K., Fujishiro, K., Tachihara, K., et al. 2020, ApJ, 899, 10
Tokuda, K., Onishi, T., Matsumoto, T., et al. 2016, ApJ, 826, 26
van der Tak, F. F. S., Lique, F., Faure, A., Black, J. H., & van Dishoeck, E. F. 2020, Atoms, 8, 15
Vastel, C., Caselli, P., Ceccarelli, C., et al. 2006, ApJ, 645, 1198
Wakelam, V., Coutens, A., Gratier, P., Vidal, T. H. G., & Vaytet, N. 2022, A&A, 666, A191
Walmsley, C. M., Flower, D. R., & Pineau des Forêts, G. 2004, A&A, 418, 1035
Ward-Thompson, D., Motte, F., & Andre, P. 1999, MNRAS, 305, 143
Ward-Thompson, D., Scott, P. F., Hills, R. E., & Andre, P. 1994, MNRAS, 268, 276
Weingartner, J. C., & Draine, B. T. 2001, ApJ, 548, 296
Whitworth, A. P., & Ward-Thompson, D. 2001, ApJ, 547, 317
Young, A. K., Bate, M. R., Harries, T. J., & Acreman, D. M. 2019, MNRAS, 487, 2853
Young, C. H., & Evans, N. J. I 2005, ApJ, 627, 293